University of Groningen, Groningen

Faculty of science and engineering

3D dust modelling of circumplanetary disks

Author:
Mark van der Keijl (S3201554)

Supervisors:
Prof. Dr. Inga Kamp
Dr. Christian Rab
Nickolas Oberg, MSc

July 5, 2019

Abstract

Planets form around young stars inside a protoplanetary disk (PPD). Theory predicts that these nascent planets can open up gaps in the protoplanetary disk, wherein a circumplanetary disk (CPD) forms around planet. To understand more about these CPDs, we build a model in which the influence of the star on the temperature structure and Far-UV radiation field of the CPD is studied. The model consists of a star surrounded by a PPD which comprises an inner and outer disk separated by a gap in which a planet surrounded by a CPD is placed. The model was built using MCMax3D, which utilizes the Monte Carlo method in order to numerically solve the radiative transfer equation of the full system (PPD + CPD). We investigate 6 models which comprises the full system (inner and outer disk), the removal of the inner disk, the removal of the inner disk and placing the CPD 10 au closer to the star, and the reduction of the planet's luminosity by an order of magnitude for all three geometrical changes. We only find a significant impact of star on the temperature of the CPD when the inner disk was removed, and the CPD was placed 10 au closer to the star. A difference in temperature was evident for both planetary luminosities between the outer edge of the side facing the star (CPDL) and the opposite side pointing away from the star (CPDR). For the default luminosity case ($L_p = 1.01 \times 10^{-2}\,\mathrm{L}_\odot$), the temperature of both sides amounted to $T_{CPDL} = (72 \pm 20)\,\mathrm{K}$ and $T_{CPDR} = (44 \pm 12)\,\mathrm{K}$. For the lower luminosity case ($L_p = 1.01 \times 10^{-3}\,\mathrm{L}_\odot$), we find $T_{CPDL} = (100 \pm 34)\,\mathrm{K}$ and $T_{CPDR} = (33 \pm 17)\,\mathrm{K}$. As for the Far-UV radiation field, we find $\chi_{CPDL} = (2.5 \pm 0.4) \times 10^4$ and $\chi_{CPDR} = (4.7 \pm 0.9) \times 10^3$ for $L_p = 1.01 \times 10^{-2}\,\mathrm{L}_\odot$, and $\chi_{CPDL} = (7.2 \pm 2.0) \times 10^4$ and $\chi_{CPDR} = (2 \pm 3) \times 10^3$ for $L_p = 1.01 \times 10^{-3}\,\mathrm{L}_\odot$. The large errors — especially for the Far-UV radiation field — are due to the lack of photons reaching the CPD. This has to do with the way MCMax3D distributes the photons and the relatively small size of the CPD. We suggest several ways to improve the MCMax3D code for CPD models as used in this thesis. Nonetheless, these 3D dust radiative transfer models provide great insight in the temperature structure and radiation field of CPDs, which are useful for studying chemistry in circumplanetary disks.

Acknowledgements

Please bear with the excruciatingly bad use of English for it's already 36 minutes past my deadline... First and foremost, I'd like to thank my sagacious supervisors! Inga, Christian, and, last but not least, Nick! Indeed, one could create the alliteration of superfluous supervisors, for who why would one need three? Well, let me tell you boy that these supervisors were absolutely not superfluous:

To Inga, for providing me with this interesting, yet demanding project. For bearing with me and not losing hope even when you discovered that I did not know what a standard deviation was. For lending me the book of Astrophysics of planet formation (which I still have to give back). And giving me proper feedback as to how I should structure my Thesis.

To Christian, for tirelessly helping me fix my code and providing me with well-founded and useful feedback for my thesis. Especially your aid during the last few weeks was incredibly helpful.

To Nick, for impersonating a German psychiatrist every time my contour plots looked like Rorschach tests. For giving me the idea to add the Glorious Red Star to the temperature plots purely because the star's temperature of 4000 K amounts to the colour red of course...

And now the mere mortals:

To Roy, for helping me out with coding, being a local Buddha, and 'fetching water' with me when our bottles were empty.

To Thom, for frequently tousling my hair when he came to pay me a visit (and of course the Kabouter dans remix).

To Roland, for he granted me the power of 'screen'. Yes indeed, this unfathomable ancient device ensured that nothing could go wrong! I am currently speculating that Roland must indeed be either a god or some kind of holy deity. He also brought candy every now and then. What a nice guy. But we mustn't forget his trusty sidekick Kevin! For with him I partook on delicious bread filled with candy! MMmmmh... delectable!

To Raul, for lending books with each other (even though Raul tends to crack the spine like a chiropractor) and musing about the wonderful world of Middle Earth.

To Jesper, for always being able to make me chuckle, for inspiring me to delve deeper into language, and for being able to recite Beowulf-esque poems that no one understands.

To Barbara, for always talking about dreams and deep philosophical stuff regardless of you being tired or not. And of course, instantly refuting any thing that does not commute with the rational mind.

And finally, to all people that I might have forgotten....

Contents

Chapter 1

Introduction

When a molecular cloud becomes unstable to gravitational collapse, protostars will start to form in the denser regions of the cloud. The structure within the cloud is inhomogeneous, meaning that its velocity and density fields exhibit turbulent behaviour. As a consequence, the collapsing cloud will have a non-zero angular momentum which will, due to the conservation of angular momentum, start to form a disk around the protostar — a *protoplanetary disk* (Armitage 2010).

Observations of such disks have indicated that protoplanetary disks can possess substructure in the form of rings, gaps, and spiral arms. The Disk Substructures at High Angular Resolution Project (DSHARP) (Andrews et al. 2018), for instance, utilized the Atacama Large Millimeter Array (ALMA), in order to map the 1.25 mm continuum of 18 protoplanetary disks. The results brought to light a prevalence of annular substructure within at least 17 of those disks. These gaps (and rings) occurred at virtually any radius in the disk ranging from 5 au till even beyond 150 au. Some gaps were shallow and clustered together; others were deep and well-stratified. Sometimes even both types were present in the same disk. These observed annular substructures bear a strong resemblance to the gaps formed in hydrodynamical simulations of planet-disk interactions (Huang et al. 2018; Zhang et al. 2018). An example of such similarities is shown in Fig. 1.1. The formation of these gaps could thus imply the presence of a planet. It has been hypothesized that such planets can form disks within its Hill sphere — so-called circumplanetary disks (CPD) (e.g., Szulágyi et al. 2018). It has been conjectured that these CPDs might be the birthplace of moons. So far, only a few possible candidates have been detected (Isella et al. 2019) and thus not very much is known about these CPDs. We therefore decided to make a model of a protoplanetary disk in which a planet with a CPD has been inserted. By testing the model for various parameters that are based on what the theory predicts, we might better understand as to why (almost) no CPDs have been detected so far. However, due to the limited amount of time assigned to this project we will mainly focus on the CPD's *temperature* and, to a lesser extent, on its *radiation field*. More specifically: what parameters affect the temperature structure in the CPD and in what way? Additionally, we will investigate how the radiation of the CPD will influence its surroundings. But before setting up this model, we must first understand how planet-disk interactions could eventually lead to CPD formation.

1.1 Planet-disk interaction

One of the most fundamental phenomena within a protoplanetary disk is *angular momentum transport* which drives processes such as planet migration, accretion and gap formation. Understanding the basic principles behind angular momentum transport is thus indispensable for understanding disk evolution.

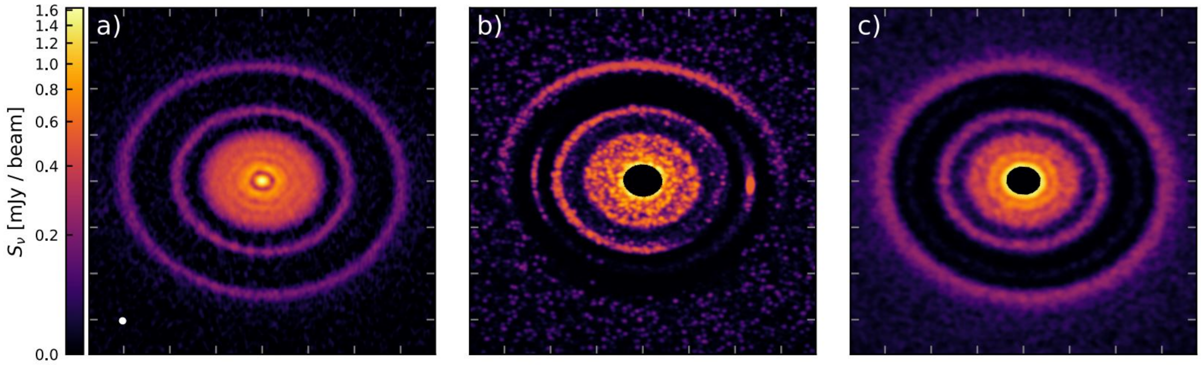

Figure 1.1: *left panel:* ALMA observation of the AS 209 protoplanetary disk displaying annular substructure. *center panel:* Result of hydrodynamical simulation with a single planet ($M_p/M_* = 0.1 M_J/M_\odot$) at 99 au. *right panel:* Result of hydrodynamical simulation using the same planet, but with different parameters for the protoplanetary disk (Zhang et al. 2018).

1.1.1 Angular momentum transport

For an isolated system, the total (global) angular momentum has to be conserved, but the *local* angular momentum, however, can change. In a geometrically thin disk, the specific angular momentum is given by:

$$l = r v_{\phi,gas} = \sqrt{G M_* r} \tag{1.1}$$

where r is the radius of the disk, $v_{\phi,gas}$ the tangential velocity of the gas, M_* the mass of the star, and G the gravitational constant (Armitage 2010). Since Eq. 1.1 is an *increasing* function of radius, the gas will *lose* angular momentum if it were to move inwards and vice versa. Because the global angular momentum has to be conserved, a local loss of angular momentum prompts a gain in angular momentum elsewhere in the disk, i.e. a certain amount of inward flow induces an equal amount of outward flow. This process is made possible by the disks' *viscosity*. In a viscous fluid, random motions generate microscopic interactions which in turn transfer momentum from the fast-moving part to the slow-moving part (Clarke and Carswell 2007; Fraternali 2019). Because the fluid elements closer to the star orbit with a higher velocity than the fluid elements further away from the star, an exchange of angular momentum naturally follows. This drives, among other things, accretion and disk evolution as local parcels of gas lose their angular momentum and spiral inwards. As gas is being accreted by the central star, the disk will — in order to conserve the total angular momentum — start to viscously spread out (Hartmann et al. 1998). Consequently, the gas surface density $\Sigma(r,t)$ (in units of g/cm^2) of the disk will decrease as function of time and radius (see Fig. 1.2). The time scale on which the surface density gradient is smoothed out by the viscosity is given by the *viscous time scale*:

$$\tau_\nu \approx \frac{r^2}{\nu} \tag{1.2}$$

where r is the disk radius and ν is the disk viscosity. The viscous time scales for protoplanetary disk generally amount to about a few million years (Armitage 2010).

1.1.2 Perturbations

When a planet is orbiting a star it will perturb the density within the disk. A subsequent shearing motion will then form spiral waves by shearing out the sound waves that emanate from

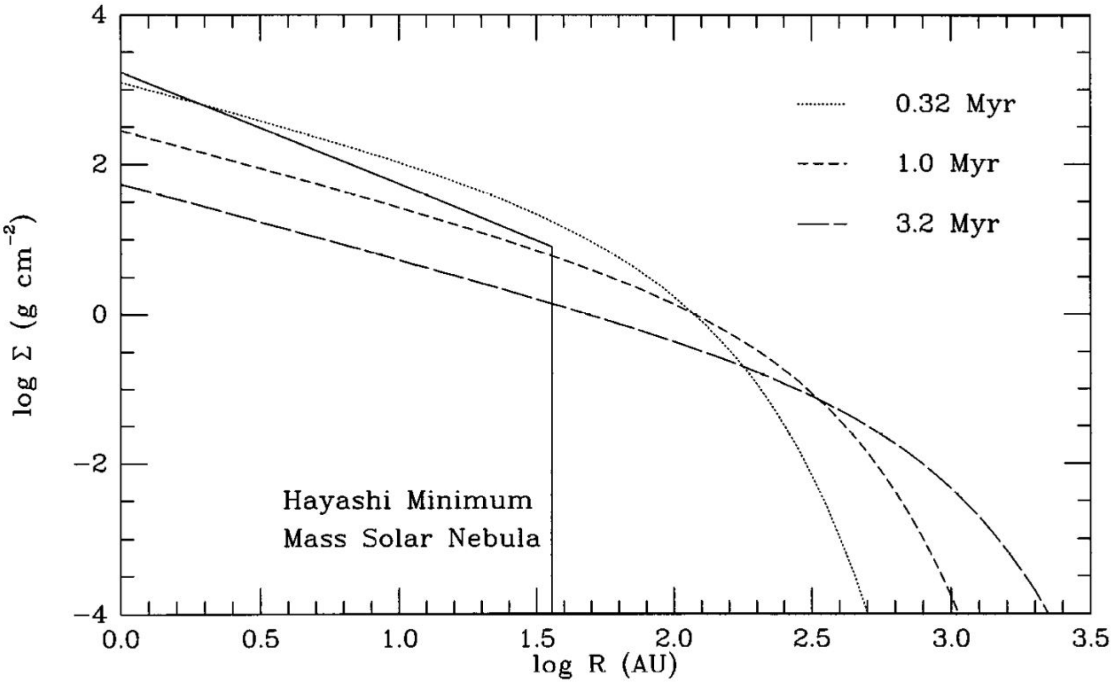

Figure 1.2: Gas surface density plotted as function of radius for 3 instances in time: $t_1 = 0.32\,\text{Myr}$, $t_2 = 1.0\,\text{Myr}$, and $t_3 = 3.2\,\text{Myr}$. Additionally, the Hayashi minimum mass solar nebula surface density distribution, $\Sigma \propto R^{-3/2}$, has been added for reference (Hartmann et al. 1998; Hayashi 1981).

the planet. Those spiral waves around the planet manifest themselves in two forms: a leading inner spiral arm and a trailing outer spiral arm. The inner spiral arm drags the planet along, accelerating it and thus increasing its angular momentum. Conversely, the outer spiral arm pulls the planet back, decelerating it and reducing its angular momentum (W. Kley and R. P. Nelson 2012; Wilhelm Kley 2019). An example of such a perturbation is depicted in the left panel of Fig. 1.3. In the right panel a schematic representation of the second perturbing factor is shown: the corotation region. The corotation region is mapped out by the particles moving in a horseshoe shaped orbit at the same speed as the planet — it is corotating with the planet. Fluid elements end up in the horseshoe region when they are close to the planet's orbital radius but have not been able to enter the planet's Hill sphere (the region around the planet in which the planet's gravitational pull is dominant over all other gravitational forces) (Armitage 2010; Richard P. Nelson 2018). Because the corotation region has a non-zero radial width, the orbiting fluid elements will have a slightly larger or smaller orbital radius depending on which side of the corotation region they are. At the U-turns the orbital radius will slightly change, prompting a change in angular momentum of the fluid elements which will consequently engender a torque acting on the planet.

In order to deeper understand the forces generated by the corotation region let us work out a simplified example. Imagine a planet with mass m_p residing in a circular orbit. Its angular momentum is given by:

$$J_p = m_p r_p^2 \Omega_p \tag{1.3}$$

Where r_p is the orbital radius of the planet and Ω_p the planet's orbital speed (in s^{-1}) (Wilhelm Kley 2019). the density asymmetries at the U-turns generate a torque, Γ_p, which is defined as

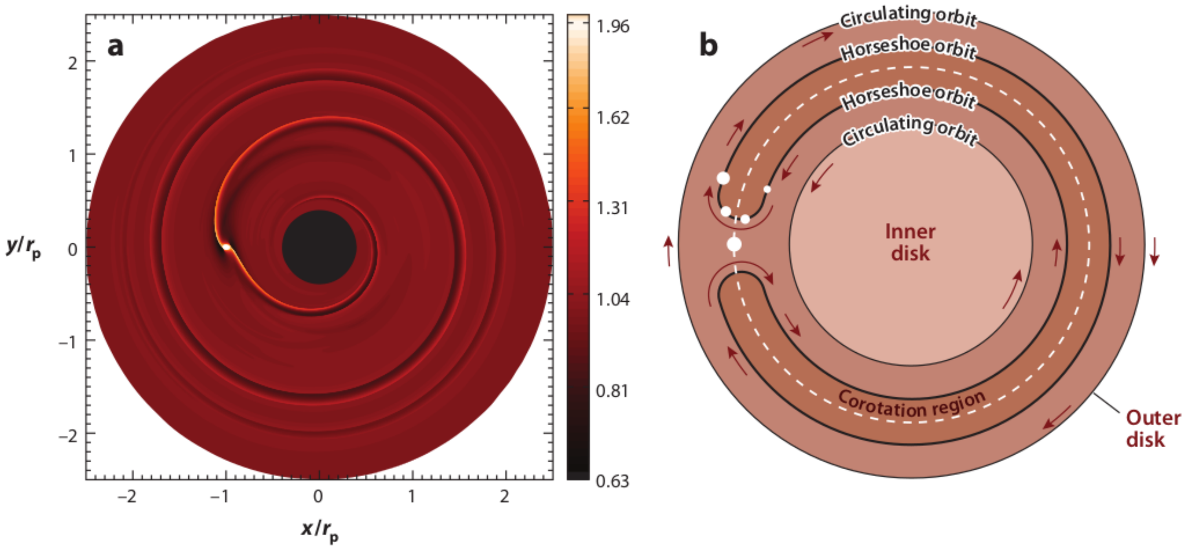

Figure 1.3: *Left panel*: orbiting planet perturbing the disk's density. Notice how the inner spiral leads and the outer spiral trails behind. The planet is the white dot (or overdensity) moving counterclockwise around the star. *Right panel*: Schematic of the flow field. The disk is subdivided into three regions: an inner disk, a corotation region resembling the shape of a horseshoe, and an outer disk. Because the system is viewed from the planet's perspective, the faster-moving inner disk rotates counterclockwise and the slower-moving outer disk clockwise. The corotation region is static since it orbits at the same speed as the planet. The fluid elements within the corotation region approach the planet (the white dot located left of the inner disk) from two sides and slightly change their orbital radius at the U-turns. As elucidated in (Eq. 1.1), the angular momentum changes as function of radius. As a result, the fluid elements will exchange angular momentum with the planet at the U-turns which will, according to Eq. 1.4, exert a torque on the planet (W. Kley and R. P. Nelson 2012).

the time-derivative of the angular momentum:

$$\Gamma_p = \frac{\mathrm{d}J_P}{\mathrm{d}t} = 2m_p\Omega_p r_p \frac{\partial r_p}{\partial t} \tag{1.4}$$

Recall that a torque is of the form $\Gamma_p = \mathbf{r_p} \times \mathbf{F}$, where $\mathbf{F}$ is the force. And because the force, due to the asymmetries, is tangential to the planet's orbit, the cross product will dictate that Γ_p will be pointing in the z-direction (coming out of Figure Fig. 1.3 towards you).
In order to find the total torque, Γ_p needs to be integrated over all individual contributions of the entire disk (assuming a flat two-dimensional case):

$$\Gamma_{tot} = -\int_{disk} \Sigma(\mathbf{r_p} \times \mathbf{F_s})_z \mathrm{d}f = \int_{disk} \Sigma(\mathbf{r_p} \times \boldsymbol{\nabla}\psi_p)_z \mathrm{d}f = \int_{disk} \Sigma \frac{\partial \psi_p}{\partial \phi} \mathrm{d}f \tag{1.5}$$

Where $\mathbf{F_s}$ is the specific gravitational force (i.e., force per unit mass) between the planet and a small surface element $\mathrm{d}f$; $\Sigma(r,\phi)$ is the surface density (g/cm^2) and ψ_p is the gravitational potential of the planet (recall the expression for the gravitation field: $\mathbf{F_s} = g = -\boldsymbol{\nabla}\psi_p$). The final expression of Eq. 1.5 was obtained by only considering the azimuthal component of the cylindrical coordinate system, i.e. $\boldsymbol{\nabla}\psi_p = \frac{1}{r_p}\frac{\partial \psi_p}{\partial \phi}\hat{\phi}$. From Eq. 1.5 we can thus infer to what extent the asymmetry changes the angular momentum of the planet. The aggregate of those two forces will bring about a change in the planet's angular momentum and consequently its orbital radius. As a result, the planet will *migrate* inwards or outwards, depending on whether it gains or loses angular momentum (W. Kley and R. P. Nelson 2012; Wilhelm Kley 2019).

1.1.3 Gap formation

Within the disk there are two main opposing forces: the viscous forces that try to smooth out the disk's surface density gradient by redistributing angular momentum, and the perturbing forces — in our case the planet — that tries to create annular substructure via exchange of angular momentum. For low-mass planets the disk remains almost unperturbed as the viscosity dominates. But for high-mass planets the perturbing effects become so strong that a gap starts to open up. This occurs when the planet orbits around the star with a larger velocity than the material exterior to the planet (larger orbital radius) and slower than the material interior (smaller orbital radius) to the planet (Bryden et al. 1999; Papaloizou and Lin 1984). Because of the viscosity, momentum from the fast-moving parts will be transferred to the slow-moving parts of the fluid (Fraternali 2019). As a result, angular momentum is transferred from the interior part to the planet which is then transferred to the exterior part. In other words, the interior material will lose angular momentum and move further inwards and the exterior material will gain angular momentum and move outwards leaving a gap in its wake. The depth and width of the gap will depend on the planet's mass and the viscosity and pressure of the disk (Armitage 2010; W. Kley and R. P. Nelson 2012).

1.2 CPD formation

At first sight, one would expect that the newly formed gap would completely impede the planet's ongoing gas accretion rate. This was assumed by the earlier models of CPD formation, in which the CPD had already completely formed before the gap opened up (e.g., Bagenal et al. 2004; Pollack and Consolmagno 1984). Later studies have shown, however, that the planet still receives a diminished, yet on-going influx of gas due to the non-vanishing viscosity within the gap (given that the viscosity is not too low) (W. Kley 1999).

Due to the reduced accretion rate, the planet starts cooling off while its mass continues to increase. As a result, the planet's hydrostatic equilibrium — the balance between the internal thermal pressure and the gravitational forces — gets disrupted as the gravitational pressure becomes dominant and the planet starts to contract (Armitage 2010; Ward and Canup 2010). Additionally, the accretion of gas will transfer angular momentum to the planet which, because of the conservation of angular momentum, causes an increase in angular velocity as the planet continues to contract. The angular velocity keeps building up until a critical rate for rotational instability is reached. At which point the most rapidly rotating material around the equator is flung out creating a so-called 'spin-out disk' (Ayliffe and Bate 2009; Korycansky et al. 1991).

If the protoplanetary disk keeps feeding the gas accretion during the contraction phase, then at one point the angular momentum of the incoming gas will be too great for it to settle on the continually shrinking planet; the gas within the Hill sphere remains orbiting around the planet and starts to form an 'accretion disk' (Canup and Ward 2002). Some earlier models have assumed that the gas accretion ends before the planet starts to contract, meaning that a pure spin-out disk will be formed. Another model suggests that the planet ceases to contract as gas continues to be supplied by the circumstellar disk, resulting in a pure accretion disk. In reality, however, a CPD is probably a combination of both processes (Ward and Canup 2010).

1.3 Irradiation of the CPD

What we have discovered so far, is that the formation of stars and its planets tend to adhere to a hierarchical structure; after a protoplanetary disk has formed around the star, a circumplanetary disk might eventually form around planets that have enough mass to accrete gas. Because a CPD is located inside a gap within the protoplanetary disk, its main source of radiation generally comes from the planet. To what extent the star illuminates the CPD relative to the planet, depends on a many variables (e.g., luminosity of the planet compared to luminosity of the star, distance between CPD and star, the optical depth of the medium etc.). The irradiation is an important factor for the temperature structure and the radiation field within the CPD. Both of these parameters greatly influence the CPD's *chemical composition* as well as its *luminosity*. Moreover, an increase in temperature will lead to an increase in viscosity, profoundly impacting the further evolution of the disk as a consequence. We will, however, only investigate how the temperature changes under varying circumstances, as its subsequent implications are outside the scope of this project. But before that, we must first address how the photons actually propagate through the medium.

1.3.1 The radiative transfer equation

One of the most pivotal physical quantities for the propagation of photons is the specific intensity I_ν, which describes the amount of energy carried in a given direction (Pinte 2015). The energy crossing a surface area $\mathrm{d}A$, in a frequency range $\mathrm{d}\nu$ and time interval $\mathrm{d}t$, and through a solid angle $\mathrm{d}\Omega$ is defined as:

$$\mathrm{d}E = I_\nu \mathrm{d}A \mathrm{d}t \mathrm{d}\Omega \mathrm{d}\nu \tag{1.6}$$

$$I_\nu = \frac{\mathrm{d}E}{\mathrm{d}A \mathrm{d}t \mathrm{d}\Omega \mathrm{d}\nu} \tag{1.7}$$

where I_ν is the specific intensity in units of erg s^{-1} cm^{-2} Hz^{-1} ster^{-1}. If a ray passes through free space (i.e., vacuum), then the intensity will remain constant:

$$\frac{\mathrm{d}I_\nu}{\mathrm{d}s} = 0 \tag{1.8}$$

In reality, however, I_ν does not stay constant as the ray always passes through some matter which will add or remove energy from beam depending on the opacity, k_ν, of the material. As a result, the expression for the energy (Eq. 1.6) must be complemented by the spontaneous emission coefficient or emissivity j_ν:

$$\mathrm{d}E = j_\nu \mathrm{d}V \mathrm{d}\Omega \mathrm{d}t \mathrm{d}\nu \tag{1.9}$$

where j_ν is in units of erg s^{-1} cm^{-3} Hz^{-1} ster^{-1}. Notice that by moving a distance $\mathrm{d}s$ with a beam of cross section $\mathrm{d}A$ maps out a volume of $\mathrm{d}V = \mathrm{d}s\mathrm{d}A$. The intensity added to the beam is then:

$$\mathrm{d}I_\nu = j_\nu \mathrm{d}s \tag{1.10}$$

Conversely, the intensity lost is given as:

$$\mathrm{d}I_\nu = -\alpha_\nu I_\nu \mathrm{d}s \tag{1.11}$$

Where α_ν is the *extinction coefficient* with units of cm^{-1}. By integrating α_ν over a distance $\mathrm{d}s$, we can derive a unitless quantity called the *optical depth* τ:

$$\mathrm{d}\tau_\nu = \alpha_\nu \mathrm{d}s \tag{1.12}$$

Another way to describe the optical depth is by using the opacity k_ν. The (radiative) opacity is defined as the capacity of matter to absorb or scatter photons as function of frequency and is given in units of cm^2/g:

$$\mathrm{d}\tau_\nu = k_\nu \rho \mathrm{d}z \tag{1.13}$$

where ρ is the density of the medium in g/cm^3 and dz the infinitesimal distance travelled into this medium in *cm* (LeBlanc 2010). The optical depth quantifies how opaque a medium is at a given frequency (LeBlanc 2010) or, more precisely, the number of mean free paths a photon can travel before being absorbed (Pinte 2015). If $\tau < 1$ the medium is *optically thin* and the photon can quite easily pass through the medium without being absorbed. If $\tau > 1$ the medium is *optically thick* and the photon can barely penetrate the medium as almost all photons get absorbed.
Adding Eq. 1.10 and Eq. 1.11 together gives us the main radiative transfer equation:

$$\frac{\mathrm{d}I_\nu(s)}{\mathrm{d}s} = j_\nu - \alpha_\nu(s) I_\nu(s) \tag{1.14}$$

1.3.2 Kirchhoff's law

Imagine a cavity containing an emitting material that is in *thermal equilibrium* with the cavity, i.e. the temperature in the cavity has one discrete value. At that point, the intensity within the cavity is equal to the Planck function ($I_\nu = B_\nu$) and does not change as function of distance ($\frac{\mathrm{d}I_\nu(s)}{\mathrm{d}s} = 0$). Rewriting Eq. 1.14 gives:

$$\frac{\mathrm{d}I_\nu}{\mathrm{d}s} = j_\nu(s) - \alpha_\nu(s) B_\nu(T) = 0 \tag{1.15}$$

$$j_\nu = \alpha_\nu B_\nu(T) \tag{1.16}$$

Where Eq. 1.16 is known as *Kirchhoff's law* which tells you that, in the case of thermal equilibrium, the emissivity j_ν of the material depends only on its temperature and the absorption coefficient α_ν. It holds as long as the medium is in local thermodynamic equilibrium (LTE).

1.3.3 The source function

We can generalize Kirchhoff's law by defining the so-called *source function*:

$$S_\nu = \frac{j_\nu}{\alpha_\nu} \tag{1.17}$$

We can thus rewrite Eq. 1.14 as

$$\frac{\mathrm{d}I_\nu(s)}{\mathrm{d}s} = \alpha_\nu(s)[S_\nu(s) - I_\nu(s)] \tag{1.18}$$

$$\frac{\mathrm{d}I_\nu(\tau_\nu)}{\mathrm{d}\tau_\nu} = S_\nu(s) - I_\nu(s) \tag{1.19}$$

Here we substituted $\mathrm{d}\tau_\nu = \alpha_\nu \mathrm{d}s$. If the medium is in LTE (i.e., $\frac{\mathrm{d}I_\nu}{\mathrm{d}s} = 0$ and $I_\nu(T) = B_\nu(T)$), the source function will equal the Planck function: $S_\nu = B_\nu(T)$.

1.3.4 Scattering

The final contribution to the radiative transfer equation is the scattering of photons which can cause a beam to either lose or gain energy; energy can be scattered away from the beam, while it can also be scattered towards the beam from the other surrounding beams. In order to implement the scattering component to the radiative transfer equation, the radiation fields in all directions and all positions need to be considered:

$$\frac{\mathrm{d}I_\nu(s,\vec{n})}{\mathrm{d}s} = -\alpha_\nu^{ext}(s)I_\nu(s,\vec{n}) + \alpha_\nu^{abs}(s)B_\nu(T(s)) + \alpha_\nu^{sca}(s)\frac{1}{4\pi}\int_\Omega \psi_\nu(s,\vec{n}',\vec{n})I_\nu(s,\vec{n}')\mathrm{d}\Omega' \quad (1.20)$$

where α_ν^{abs} and α_ν^{sca} are the absorption and scattering cross section, respectively. Adding these two components together gives the extinction cross section: $\alpha_\nu^{ext} = \alpha_\nu^{abs} + \alpha_\nu^{sca}$. Finally, The scattering phase function, $\psi_\nu(s,\vec{n}')$, takes the random directions of scattered photons into account by computing the probability that a photon will be scattered from direction $\vec{n}$ to a direction $\vec{n}'$. This severely complicates the solution of the radiative transfer equation, as it needs to be simultaneously solved for all rays and along all directions in order to obtain the intensity $I_\nu(s,\vec{n})$.

1.3.5 The complexity of radiative transfer

The previous sections have expounded the various facets of the radiative transfer equation. The complexity in solving this equation arises when the parameters have to be frequently recalculated. This happens in optically thick regions, where the density of the medium is so high that the photon can only travel an incremental distance before being scattered again. Conversely, in optically thin regions, the photons barely interact with the medium and can therefore propagate without too much interruption. The complexity becomes more apparent if we combine all hitherto treated components into one equation:

$$\frac{\mathrm{d}I_\nu(s)}{\mathrm{d}s} = \alpha_\nu^{ext}(s)[S_\nu(s) - I_\nu(s)] \quad (1.21)$$

where

$$S_\nu(s) = S_\nu^{emission}(s) + S_\nu^{scattering}(s) \quad (1.22)$$

$$= \alpha_\nu^{abs}(s)B_\nu(T(s)) + \alpha_\nu^{scatt}(s)\frac{1}{4\pi}\int_\Omega \psi_\nu(s,\vec{n}',\vec{n})I_\nu(s,\vec{n}')\mathrm{d}\Omega' \quad (1.23)$$

The problem lies in the fact that Eq. 1.21 and Eq. 1.22 are coupled, as the scattering term of the source function depends on the specific intensity $I_\nu(s,\vec{n}')$. In order to get a proper result, Eq. 1.21 and Eq. 1.22 thus need to be solved together (Pinte 2015).

1.4 Continuum radiative transfer

The composition of protoplanetary disks consists of gas and dust of which dust only makes up for $\sim 1\%$ of the total mass. Even though the amount of dust is nugatory compared to the amount of gas, it does, in fact, play an important role in setting the temperature of the disk. Dust grains heat up when they absorb a photon and, conversely, cool down when re-emit a photon, but unlike gas, which absorbs and emits only at specific *discrete* wavelengths, dust interacts with the stellar radiation on a *continuous* range of wavelengths. The continuum opacities are thus dominated by the dust. Dust grains absorb, scatters and polarizes more efficiently at shorter wavelengths, and re-emits more efficiently at longer wavelengths (Pinte 2015). As depicted in Fig. 1.4, the capability of the dust to absorb radiation happens predominantly in the wavelength range up to the optical (i.e., up to $\lambda \approx 0.8\,\mu$m). The amount of absorbed radiation sets the dust temperature and dictates the amount of radiation it subsequently emits. How much radiation is absorbed and scattered depends on the geometry of the disk, the properties of the dust and the intensity of the stellar radiation (Pinte 2015).

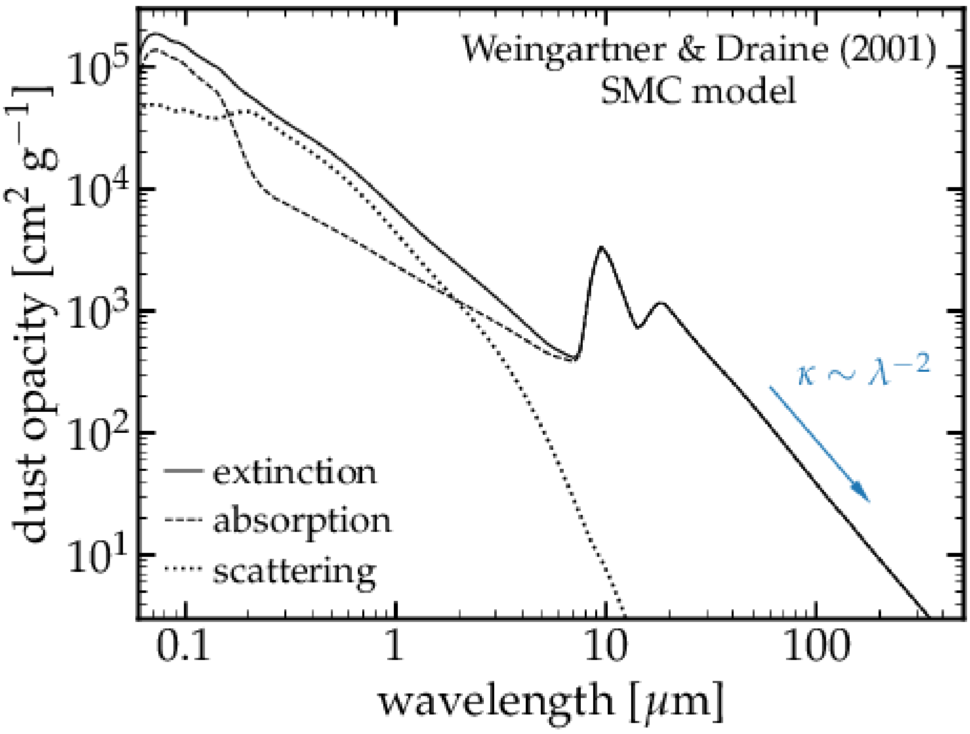

Figure 1.4: Dust opacity plotted as function of wavelength for the Small Magellanic Cloud (SMC) grain size distribution model (Ma et al. 2019; Weingartner and B. T. Draine 2001).

1.4.1 Dust grain dominance

The abundance, or rather the density of the dust grains will determine whether a region is optically thin or thick; in optically thin regimes, the radiation field is dominated by the stellar radiation field which also sets the dust temperature. Conversely, in optically thick regions the stellar radiation cannot penetrate through the dense slab of dust grains as they get immediately absorbed by the outer layer. This "self-shielding" causes the dust-grains within that region to be only heated by its own infrared emission, which is significantly less energetic than the stellar flux (Bruce T. Draine 2011; Maciel 2013; Pinte 2015).

Aside from the amount of grains, the properties of the dust (i.e., the opacity law see Fig. 1.4) are also an important factor in setting the temperature. Smaller grains have a more steep opacity law between the optical and mid-infrared regimes. Because they are not good emitters in the mid-infrared, they need to reach rather high temperatures in order to emit the absorbed energy. Larger grains, on the other hand, have a flat opacity law; they absorb less stellar radiation and re-emit more in the infrared. As a result, the smaller grains will attain a much higher temperature than the large grains (Pinte 2015; Woitke, Min, et al. 2016a). For t

1.5 Scientific goal

The main aim is thus to investigate the impact of the stellar radiation on the temperature structure and the radiation field of the CPD under various circumstances. The theory in this chapter served to provide all the knowledge required for understanding the subsequent results. In Chapter 2, we describe the method that sets up our model and calculates its temperature and radiation field. Chapter 3 has been subdivided into 2 sections: the technical part and the scientific part. The technical part treats the experimental nature of this project by testing which set-up yields the most accurate results within a reasonable simulation time. The scientific part then uses this specific set-up for 6 different models. Finally, chapter 4 summarizes the main findings and discusses its implications.

Chapter 2

Methodology

Let's get this show on the road!

MCMax3D

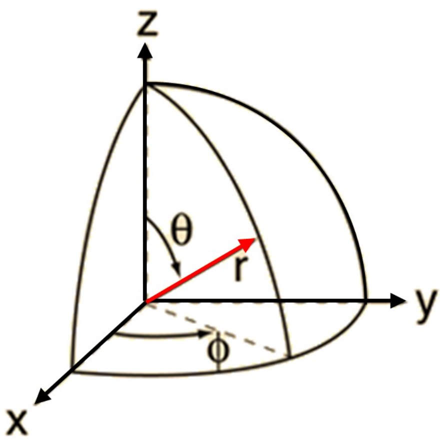

Figure 2.1: Schematic of the spherical coordinate system. The midplane (i.e. the plane of the planet's orbit) is located at $\theta = \frac{\pi}{2}$ (or $z = 0$). The midplane is a cardinal point of this project and will often be referred to.

The program that is used for setting up the model is MCMax3D (Min, Bouwman, et al. 2016; Min, Dullemond, et al. 2009). As the name suggests, this program generates the disk model in 3D space using a spherical coordinate system (see Fig. 2.1) which will later be converted into Cartesian coordinates for the plotting. The motive for opting for MCMax3D, however, lies not so much in its ability to operate in 3D as in its flexibility in building up a planetary system; the protoplanetary disk is subdivided into so-called *zones*, all of which have their own parameter space and are thus independent from one another. A zone is essentially a component of the whole disk-system that is (in general) physically separated from any other zone. The most notable parameters of the zones are the dust mass (M_{dust}), the inner (R_{in}) and outer radius (R_{out}), and its positional arguments (xyz). If no positional arguments are specified then the zone will regard the Origin of the spatial grid as its center. For the zone that constitutes the CPD, however, a specification of its positional arguments are required in order to place the zone around the planet that orbits the star at some radius. Moreover, the parameters of the zones can be procedurally changed to probe the CPD's temperature and radiation field under varying circumstances (e.g., place the CPD closer to the host star).

The model that MCMax3D builds is, unlike hydro-dynamical simulations, completely *static*, meaning that no geometrical structures that make up the model move. This serves the purpose of investigating the radiative influences within the disk model. As explained in the introduction (Sect. 1.3), solving the continuum radiative transfer in a diverse system like a protoplanetary disk is exceedingly complex. MCMax3D tackles this problem by utilizing the *Monte Carlo* method.

2.1 Monte Carlo

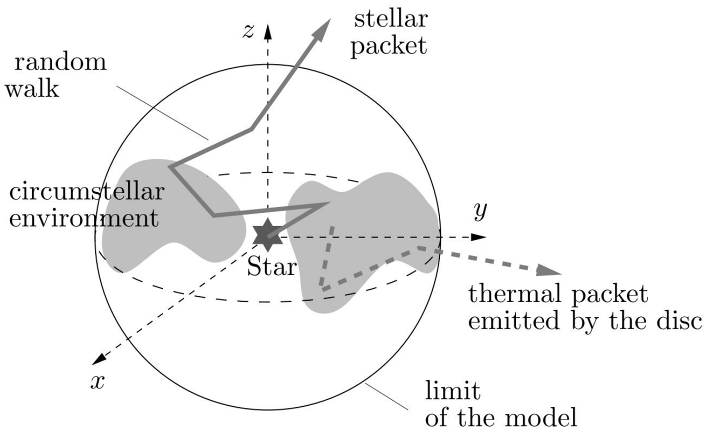

Figure 2.2: Schematic of the 3D random walk of the photon packet. The full line represents a photon packet emitted from the star, and the dashed line a photon packet emitted by the dust (in the disk) (Pinte 2015).

The Monte Carlo method solves the continuum radiative transfer equation by randomly drawing photon packets from a probability distribution function in an iterative way. Each photon packet is individually followed as it is scattered, absorbed and re-emitted until it eventually leaves the system (see Fig. 2.2). When a photon packet gets absorbed, it transfers its energy to the cell (i.e., the dust grains in that cell), heating it as a consequence. This absorption process destroys the photon packet, but its transferred energy will be re-emitted in the next iteration. The scattering of a photon packet will only change the propagation direction of the incident photon. Because this procedure relies on 'randomness', some regions receive less photons than others leading to noisy results, i.e. Monte Carlo noise. This drawback is inherent to the Monte Carlo method due to its probabilistic nature, and can be reduced by increasing the number of sampled photons at the cost of longer computation times. Furthermore, for a very large probability of interaction (e.g., regions with a very high optical depth), the photon packet takes a long time to propagate through the medium as it constantly interacts with the medium. Conversely, a very low probability of interaction causes the photon to 'freely' propagate through the medium, producing no data about that region as a consequence. The big advantage of the Monte Carlo method, however, is that it works very well in 3D as it accurately traces the propagation of the photons (Pinte 2015).

2.2 Model Set-up

For this particular project, we classify three zones: the inner disk (zone 1), the outer disk (zone 2) and the CPD (zone 3). Additionally, the host star and the planet are both regarded as light sources as they both emit photons required for the Monte Carlo simulation. In terms of radial size, the inner disk extends from an inner radius of $R_{in} = 0.4\,\mathrm{au}$ to an outer radius of $R_{out} = 18\,\mathrm{au}$, and the outer disk extends from an inner radius of $R_{in} = 22\,\mathrm{au}$ to an outer radius of $R_{out} = 500\,\mathrm{au}$. The void in between the outer edge of the inner disk and the inner edge of the outer disk constitutes a *gap* in which the planet has been placed at $x = 20\,\mathrm{au}$. Finally, the third zone (i.e., the CPD) surrounds the planet ($R_p = 0.54\,\mathrm{R}_\odot = 2.5\times10^{-3}\,\mathrm{au}$) with an inner radius of $R_{in} = 10^{-3}\,\mathrm{au}$ to an outer radius of $R_{out} = 1\,\mathrm{au}$ relative to the planet's location. Furthermore, for each zone the *number of grid points* needs to be specified in order to define the zone's resolution. We distinguish three types of grid points according to the spherical coordinate system: the azimuthal grid points (ϕ), the polar grid points (θ), and the radial grid points (r).[1] Together they comprise a complete sphere in which a CPD or protoplanetary disk structure can be formed.

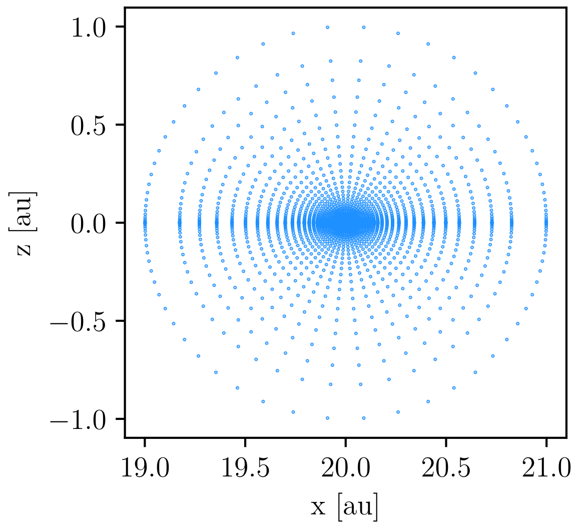

Figure 2.3: Scatter plot of the the radial and polar grid points for the two values of ϕ which are on one line with the star and the planet, i.e. (z,y) = (0,0) (see left panel of Fig. 2.4). The number of grid points used in this example for the azimuthal, polar and radial components amount to 60, 50 and 60, respectively. These grid points belong to zone 3 (the CPD) for which the planet is located in the center.

In Fig. 2.3 the distribution of the grid points is displayed for the two values of ϕ that are in line with the star and planet. This grid point configuration is also the template for the plots that will be shown in the Results section. Notice how the grid points are logrithmically spaced; they cluster around their Origin and take continuously larger steps as they move away from it. The spherical components have been converted into Cartesian coordinates to facilitate the plotting routine. The radial grid points are the lines that begin close to the planet (located at (x,z) = (20,0)) and move logrithmically outward. The number of polar grid points determine in how many slices each semicircle will be subdivided (50, in this case). The polar grid points start from the top of the sphere ($\theta = \frac{\pi}{2}$ or $z = 1$ in this plot) and end at the bottom ($\theta = \frac{3}{2}\pi$ or $z = -1$).

In Fig. 2.4, the dust density structure of the complete system is depicted on a Cartesian coordinate grid in the xz-plane (left panel) as well as a midplane cut in the xy-plane (right panel). The star is located in the center ($(x, y, z) = (0, 0, 0)$) and is enveloped by a protoplanetary disk. The protoplanetary disk has been split in two by the gap opened up by the planet. Starting

[1] In the code the azimuthal, polar and radial grid points are referred to as **np**, **nt** and **nr**, respectively.

from the star (at $(x,z) = (0,0)$ or $(x,y) = (0,0)$) and moving outwards along the positive x-axis, we come across three zones in the following order: The inner disk (zone 1), the CPD (zone 3) and the outer disk (zone 2). The CPD is labeled as zone 3, since it was last added to the system. Notice that the density gradient (and thus the mass distribution) in each zone is such as explained in the introduction; the bulk of the mass resides in the midplane (all x and y-values at $z = 0$) which then exponentially decreases as function of z (Woitke, Min, et al. 2016b). This slice also clearly displays the flaring behaviour of both the protoplanetary disk and the CPD. Notice how the density within the midplane barely changes as function of radius ($r = \sqrt{x^2 + y^2}$). The difference in density for each zone is brought about by the differing mass assigned to each zone.

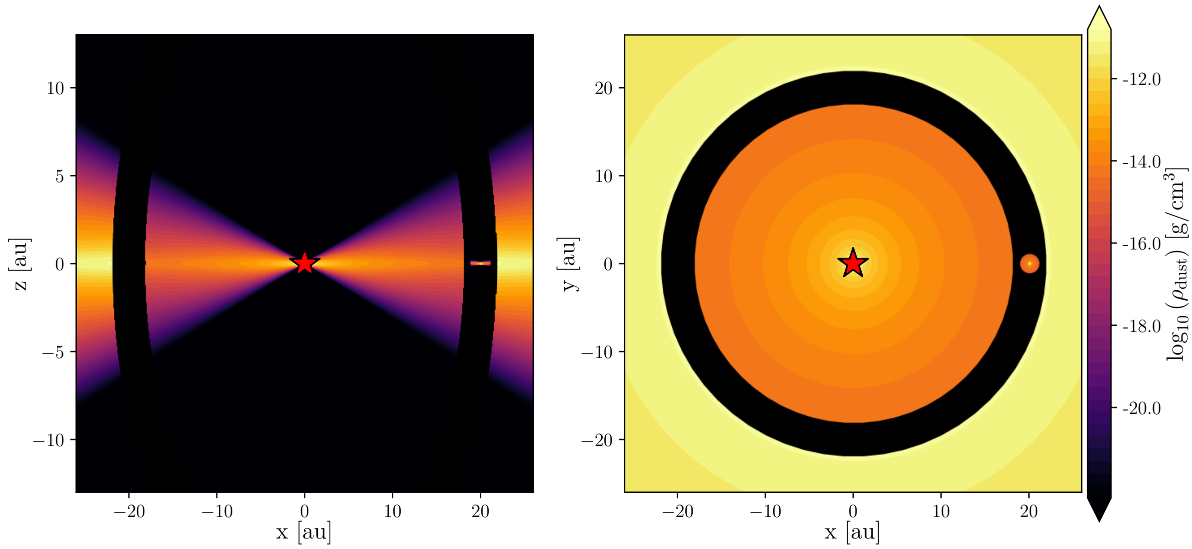

Figure 2.4: Dust density contour of the protoplanetary disk with a planet and CPD placed in the gap (at $x = 20\,$au). *Left:* xz-plane of the protoplanetary disk with CPD. *Right:* xy-plane in the midplane, i.e. at $\theta = \frac{\pi}{2}$.

Quantity	**Symbol**	**Star (star01)**	**Planet (star02)**
Temperature	T	4000 K	2500 K
Luminosity	L	$1.01\,\mathrm{L}_\odot$	$1.01 \times 10^{-2}\,\mathrm{L}_\odot$
Radius	R	$2.09\,\mathrm{R}_\odot$	$0.54\,\mathrm{R}_\odot$
Mass	M	$1\,\mathrm{M}_\odot$	$1.91 \times 10^{-2}\,\mathrm{M}_\odot$
Position	x,y,z	(0,0,0) au	(20,0,0) au

Table 2.1: Main parameters used for the star and planet.

The parameters of the system (such as the previously mentioned number of grid points, radius of each zone etc.) can be changed in the *input.dat* file. In Table 2.1 a list of the parameters — in default settings — for the planet and star are listed. The star's parameters are based on the spectrum of a T Tauri star. For the planet we assume 1% accretion luminosity (i.e., it is a young accreting planet) which is added to the total photospheric luminosity of the planet (hence 1.01×10^{-2} instead of 10^{-2}). It is important to be consistent with this so as to keep the photospheric emission for both models the same. The accretion luminosity for both the star and

Quantity	**Symbol**	**Inner disk (zone1)**	**Outer disk (zone2)**	**CPD (zone3)**
Inner radius	R_{in}	0.4 au	22 au	3×10^{-3} au
Outer radius	R_{out}	18 au	500 au	1 au
Exp. decline radius	R_{exp}	18 au	100 au	21 au
Dust mass	M_{dust}	$2 \times 10^{-5}\,\mathrm{M}_\odot$	$1 \times 10^{-4}\,\mathrm{M}_\odot$	$10^{-10}\,\mathrm{M}_\odot$
Radial grid points	nr	60	60	60
Polar grid points	nt	50	50	50
Azimuthal grid points	np	60	60	60
Radial density gradient	r^α	$\alpha = -1$	$\alpha = -1$	$\alpha = -1$
Flaring	r^β	$\beta = 1.15$	$\beta = 1.15$	$\beta = 1.15$
Position	x,y,z	(0,0,0) au	(0,0,0) au	(20,0,0) au

Table 2.2: Parameters used for each zone.

planet should increase the strength of the UV field. Finally, the planet's coordinates have been specified to manually place it at the desired location.

In Table 2.2 all the relevant parameters for each zone are listed. As previously mentioned, each zone can be individually changed, which offers quite a bit of freedom in building up a protoplanetary disk structure. The coordinates for the CPD have been specified in order to place it around the planet. The parameters R_{in} and R_{out} set the starting and end point of each zone in units of au, respectively. R_{exp} determines at what radius the surface density will start to decline exponentially. M_{dust} sets the total dust mass which MCMax3D also uses to calculate the gas mass by simply multiplying it with a factor 100 (since a gas-to-dust mass ratio of 100 is assumed). Notice how the dust mass of the CPD is considerably lower than that of the other zones. This has been done to account for the smaller volume and by keeping the CPD optically thin enough so that photons can pass through more easily. *denspow* and *shpow* determine what power law the zone should follow as function of radius for the radial density gradient ($\propto r^{-1}$) and degree of flaring ($\propto r^{1.15}$), respectively. Finally, nr, nt and np represent the number of radial, polar and azimuthal grid points, respectively. The reading and processing of the MCMax3D data is done with Python.

Chapter 3

Results

Using MCMax3D for this particular end has never been done before, giving this project a highly experimental nature. The Results section has, therefore, been split up into two sections: The *Technical* (Sect. 3.1) and the *Scientific* (Sect. 3.2) part. In Sect. 3.1, a default model will be put forward whose number of grid point and number of photons will be procedurally changed. The goal is to find the best configuration for the amount of photons and spatial grid points required to achieve accurate results within an acceptable amount of computation time. In Sect. 3.2, this configuration will be used for 6 different models which comprise a change in the CPD's luminosity and position as well as the complete removal of the inner disk. The CPD's temperature and radiation field for each model will subsequently be investigated.

3.1 Technical tests

MCMax3D has two input parameters that can significantly influence the accuracy of the results as well as the computation time of the simulations, namely the amount of generated *photons* and *grid points*. For this project both these input parameters have been divided into three modes: the low amount (**L**), the high amount (**H**), and the very high amount (**Hmax**). How this translates into the number of photons and grid points is shown in table Table 3.1. We have chosen the name Hmax since that is the absolute maximum number of photons MCMax3D can generate due to its 32 bit limit ($2^{31} \approx 2.1 \times 10^9$). The same is true for the number of grid points: originally we had set them at (ϕ, θ, r)= (240, 200, 240) to continue the trend of doubling the number grid points, but at that point the output became larger than 2 Gb which started to cause problems. This limit is due to the routine that writes the fits files, but the details of this caveat still need to be further investigated.

Mode	**Number of photons**	**Number of grid points**
Low (L)	10^7	(ϕ, θ, r)= (60, 50, 60)
High (H)	10^9	(ϕ, θ, r)= (120, 100, 120)
Very High (Hmax)	2.1×10^9	(ϕ, θ, r)= (200, 200, 200)

Table 3.1: The modes and their corresponding number of photons and grid points.

The number of grid points in Table 3.1 are displayed in a (ϕ, θ, r) format, multiplying these dimensions with each other gives us the total number of grid points:

$$\mathrm{L} = 60 \times 50 \times 60 = 1.8 \times 10^5 \,\text{gridpoints} \tag{3.1}$$
$$\mathrm{H} = 120 \times 100 \times 120 = 1.44 \times 10^6 \,\text{gridpoints} \tag{3.2}$$
$$\mathrm{Hmax} = 200 \times 200 \times 200 = 8 \times 10^6 \,\text{gridpoints} \tag{3.3}$$

3.1.1 Assessing the quality of each configuration

With these three modes and its two variable input parameters, a total of nine configurations can be realized. The accuracy of each configuration will be assessed by looking at the noise level of the temperature in the CPD. In our set-up (Fig. 2.4), the CPD has a side facing the star (i.e., the left side of the CPD) and a side pointing away from the star (i.e., the right side of the CPD). The importance of these two sides will be further explained in Sect. 3.2. For now, we are only interested in the noise-level as a means to quantify the accuracy of each configuration. In Fig. 3.1, a schematic depicts how the CPD is split into two semicircles: the left and right CPD. The two radii in line with the star (located on the left) are called *CPDL* (at $\phi = \pi$) and *CPDR* (at $\phi = 0$). The ϕ-values extend around CPDL and CPDR such that one third of their respective semicircle is swept out. These areas (or sextants) are highlighted in brown and are symmetric around CPDL and CPDR. Every ϕ slice has the same number of radial grid points that maps out the radius of the disk at a given angle. The idea is to reduce the Monte Carlo noise within the two sextants by averaging over the multiple ϕ-values for each radial grid point. The obtained average temperatures will then be regarded as the temperature belonging to CPDL and CPDR. We could have chosen to average over all ϕ-values so as to reduce the Monte Carlo noise even further, but that would smooth out the possible temperature difference between CPDL and CPDR which is important for Sect. 3.2.

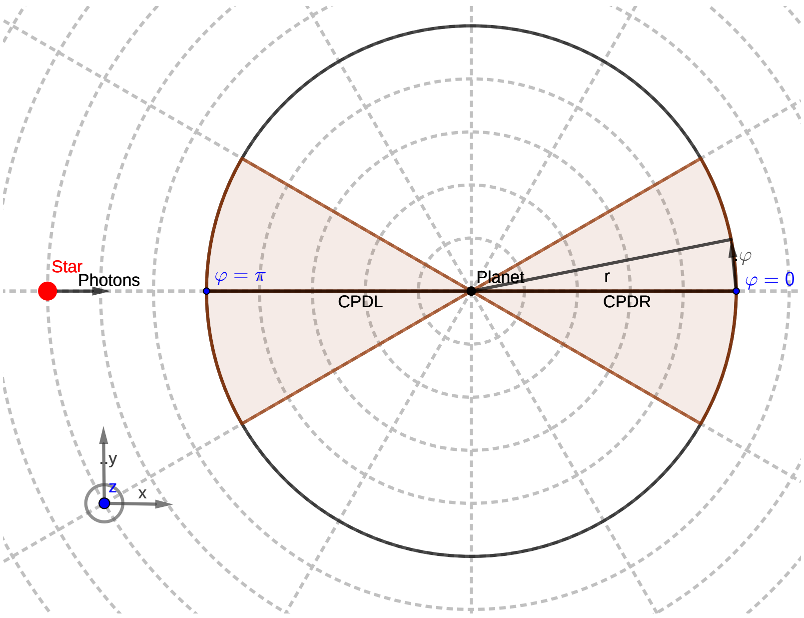

Figure 3.1: Schematic of midplane cut ($z = 0$) in the xy-plane centered around the planet (*not on scale*): this schematic serves to get a better grasp of how the temperature plots are created. In the bottom left corner the orientation of the Cartesian coordinate system is displayed (z comes out of the paper and goes in to the paper since we are in the midplane). The CPD is delineated as the black circle with the planet in its center. The star is located on the left.

By process of elimination, the configuration that gives rise to the most accurate and least time consuming results will be selected. We will first start with finding the most optimal number of photons while keeping the number of grid points fixed. The selected number of photons will then be tested for the three modes of grid points until the best configuration is found. 6 configurations will thus explicitly be compared with one another in the main text, while all 9 configurations are more succinctly compared in Table 3.2.

Configuration	**Photons**	**Grid points**	$\mathcal{L}_i$	$\mathcal{L}_f$	$\mathcal{R}_i$	$\mathcal{R}_f$
		(ϕ, θ, r)	Relative error in temperature			
LL	10^7	(60, 50, 60)	123%	71 %	77%	67%
LH	10^7	(120, 100, 120)	434%	132%	159%	74%
LHmax	10^7	(200, 200, 200)	312%	138%	266%	126%
HL	10^9	(60, 50, 60)	7%	6%	8%	4%
HH	10^9	(120, 100, 120)	11%	7%	13%	10%
HHmax	10^9	(200, 200, 200)	27%	17%	22%	9%
HmaxL	2.1×10^9	(60, 50, 60)	5%	5%	4%	3%
HmaxH	2.1×10^9	(120, 100, 120)	10%	6%	9%	9%
HmaxHmax	2.1×10^9	(200, 200, 200)	17%	17%	13%	12%

Table 3.2: Relative errors of the initial and final point radial grid point of the left ($\mathcal{L}_i$ and $\mathcal{L}_f$) and right ($\mathcal{R}_i$ and $\mathcal{R}_f$) disk half of the CPD.

3.1.2 Number of emitted photon packages

Selecting the optimal amount of photons is all about balance: using a lot of photons leads to a longer computation time, while using too few will inevitably lead to inaccurate results. We are therefore looking for the number of photons that can provide a reasonable accuracy within an acceptable computation time. The following three configurations will be put to the test: LL, HL, HmaxL. Where we use a low number of grid points for all three cases to minimize the required computation time. The total amount of ϕ-values for these three configurations amount to 60 (see Table 3.1), meaning that the two sextants each comprise 10 ϕ-values. The temperature values of the left and right sextant are plotted as function of radial grid points, which are subsequently overplotted by its average temperature and the corresponding error bars (the standard deviation). Through the calculation of the standard deviation (i.e., the error), the noise can be quantified and used for evaluating the accuracy of the various configurations.

To show the impact of the chosen number of photons on the results, the radial temperature profiles of configuration LL and HL are displayed in Fig. 3.2 and Fig. 3.3, respectively. In the LL configuration, the average temperature decreases quite erratically as function of radial grid points, which is indicative of substantial noise: the first data point of CPDL and CDPR display a relative error of 123% and 77%, respectively. In the last data point of CPDL and CPDR, we notice a decrease in noise with a relative error of 71% and 67%, respectively. In HL, the decline of the average temperature values proceed more smoothly as evidenced by their significantly smaller errors: a relative error of 7% and 6% for the first and last data point in CPDL, and a relative error of 8% and 4% for the first and last data point in CPDR. HmaxL is not displayed, but is very similar to HL with a relative error of 5% and 5% for the first and last data point in CPDL, and a relative error of 4% and 3% for the first and last data point in CPDR. HL and

Hmax are thus almost equally accurate. Their relative computation time, however, is not at all similar as HmaxL takes around twice as long to finish.[1] For the sake of time, we therefore decided to stick with 10^9 photons (H).

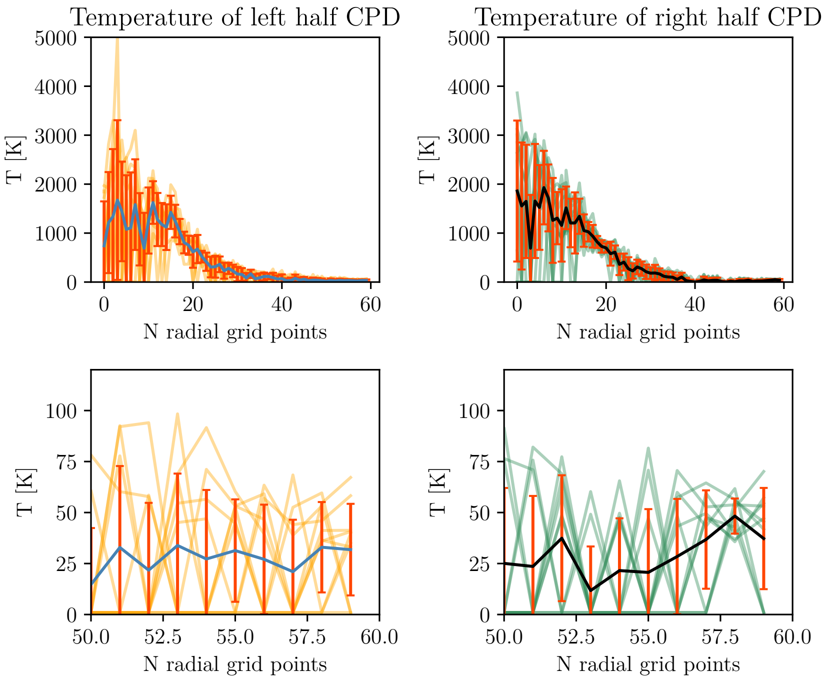

Figure 3.2: Radial temperature profile for LL (10^7 photons): the yellow and green lines are all the temperatures belonging to the ϕ-values within the left and right sextant, respectively. The blue (left) and black (right) line represent the average temperature, both of which are complemented with the standard deviation in the form of orange-red error bars. *Top left:* radial temperature profile as function of radial grid points for the left side of CPD (CPDL). *Bottom left:* zoom-in of top left panel for a clearer picture of the temperature behaviour at outer edge of CPDL. *Top right:* radial temperature profile as function of radial grid points for left side of CPD (CPDR). *Bottom right:* zoom-in of top left panel for a clearer picture of the temperature behaviour at outer edge of CPDR.

[1] Note that computation time depends heavily on how many cores we could use during the simulations which in turn depends on how many people were using the computer clusters. Hence this factor 2 difference is a rough estimate, but still of significant value in determining the best configuration.

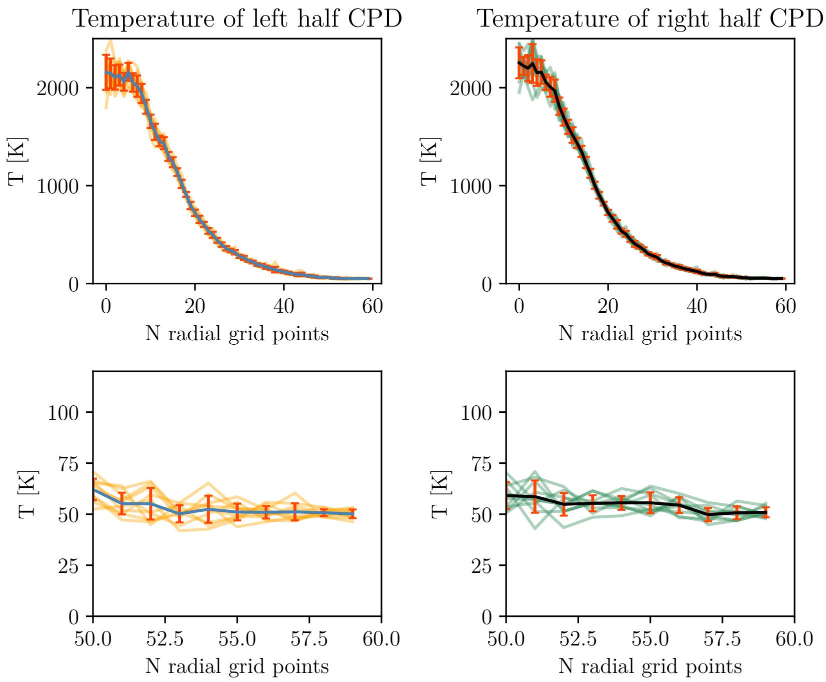

Figure 3.3: Radial temperature profile for HL (10^9 photons): The plotting was carried out using the exact same procedure as Fig. 3.2.

3.1.3 Number of spatial grid points

Now that we have settled on the photon abundance, we can vary the number of grid points while keeping the photon abundance fixed at H. Since we have already displayed the HL plot, only HH and HHmax will be shown here.

The plots are displayed below (Fig. 3.4 and Fig. 3.5) and both seem quite a bit noisier than HL (Fig. 3.3). The reason for this extra noise is because an increase in the number of grid points leads to a smaller volume element per grid point. If the volume element decreases, then the chance of a photon hitting it will also decrease, resulting in more noise. This means that a lower number of grid point leads to more accurate results at the cost of a lower resolution. The latter case is definitely not unimportant, as a higher resolution shows more structural details. However, in the light of maximizing the accuracy of the results, a low number of grid points is deemed necessary.

We have thus found that the errors in the H and Hmax level of photons are quite similar with Hmax being slightly more accurate. Their accuracy both decreases for an increasing number of grid points. As a result, the most accurate results are provided by the HmaxL configuration, but considering its long computation time we we opted for **HL** as the most convenient configuration.

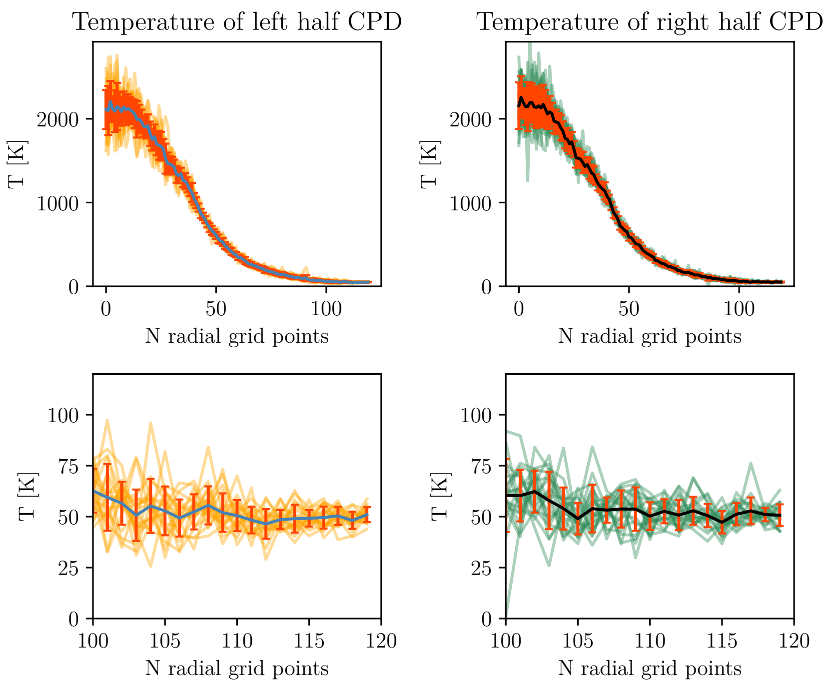

Figure 3.4: Radial temperature profile for HH ((ϕ, θ, r)= (120, 100, 120)): The errors seem slightly higher compared to HL.

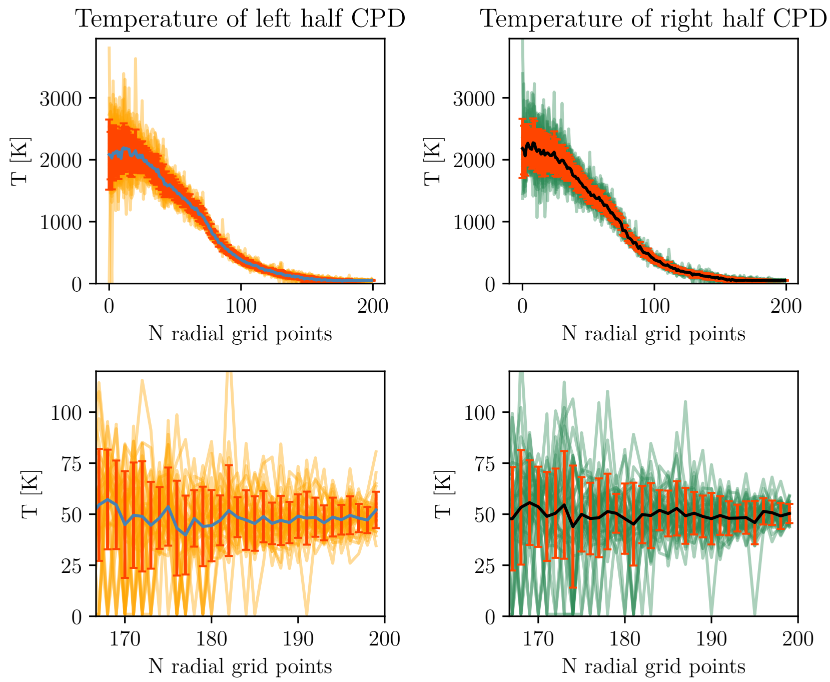

Figure 3.5: Radial temperature profile for HHmax ((ϕ, θ, r)= (200, 200, 200)): Here the errors are significantly larger than HH and HL.

3.2 Scientific tests

In this section, we will investigate the influence of the star on the CPD's temperature gradient and radiation field for various models. Additionally, we will also briefly discuss the impact of the CPD on the surrounding inner and outer disk.

The models that we shall be testing are based on the following phenomena: planets can have different luminosity; some protoplanetary disk are devoid of inner disks, so-called transitional disks (Kim et al. 2013); and planets can orbit the star at different orbital radii, influencing their received stellar flux. Considering these factors, we get 3 main configurations:

1. The full system as depicted in Fig. 2.4.
2. The full system without the inner disk.
3. The full system without the inner disk and the planet plus CPD placed at a 10 au (instead of 20 au) distance from the star.

Each of these configurations will be tested for two planetary luminosities: The default luminosity ($L_p = 1.01 \times 10^{-2}\,\mathrm{L}_\odot$) and the luminosity lowered by an order of magnitude ($L_p = 1.01 \times 10^{-3}\,\mathrm{L}_\odot$). For the first configuration, the influence of the CPD on the inner and outer disk will also be examined.

The CPD's dust density (and thus the gas density) are fixed for all models (Fig. 3.6). The importance of the dust density should not be forgotten, however, as it dictates, among other things, how much radiation penetrates and thus what temperature the CPD will ultimately attain.

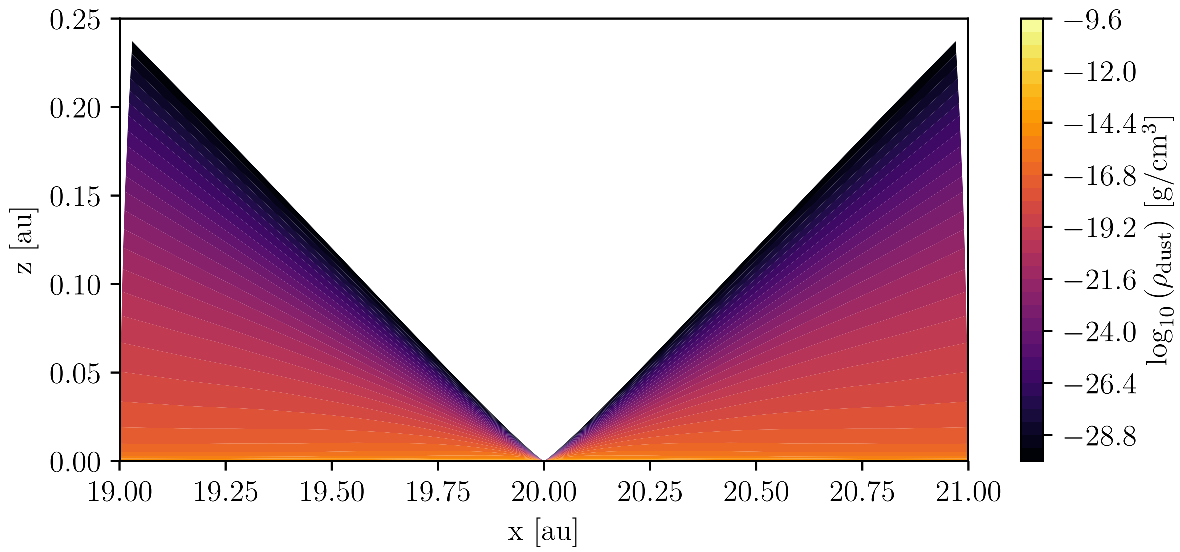

Figure 3.6: Dust density of the CPD in the xz-plane, where z corresponds to the height of the disk. Because the disk is symmetric along the x-axis, only the upper half of the disk is depicted. The planet is located at 20 au, and is enveloped by the CPD with a radius of 1 au whose z-values increase with increasing radius (x) due to flaring. Notice how the density is maximal around the midplane and that it steeply decreases as function of z.

3.3 Configuration 1: Full system

The temperature section consists of a three-way approach: first, the 3D temperature structure of the full system — inner disk (if present), outer disk and CPD — will be depicted via a cut through the xz-plane and and a cut through the midplane (xy-plane). Next, a scatter plot of the radial temperature profile in the disk midplane — in line with the star and planet ($\phi = 0$ and $\phi = \pi$; see Fig. 3.1) — will be studied for all three zones. The impact of the CPD on the inner and outer disk will also be investigated. After that, we zoom in on the left and right side of the CPD and apply the exact same procedure as described in Sect. 3.1.1 and Fig. 3.1. Finally, CPDL and CPDR will be plotted together to infer the star's impact on the left and right side of the CPD.

3.3.1 Temperature

The temperature of the full system is depicted in Fig. 3.7. The default settings (as shown in Table 2.1 and Table 2.2) have been used for this configuration. The CPD is thoroughly heated due to its low density and highly luminous planet ($L_p = 1.01 \times 10^{-2}\,\mathrm{L}_\odot$); the planet's photons easily cover the whole CPD until they irrevocably strand in one of the surrounding, more optically thick zones. Notice how these photons still have plenty of energy to significantly heat up a small area of the surrounding inner and outer disk. Conversely, no stellar photons really penetrate the inner disk, implying that the CPD is solely heated by the planet. For the lowered luminosity case $L_p = 1.01 \times 10^{-3}\,\mathrm{L}_\odot$ in Fig. 3.8, the planet heats the CPD and surrounding inner and outer disk to a considerably lesser extent. As a side note: since MCMax3D does not consider background radiation its lowest temperature outputs amounts to $-1\,\mathrm{K}$ (presumably, because those grid points did not receive any photons, hence it was undefined). To overcome this non-physical value, we capped the lowest temperature at that of the Cosmic Microwave Background $T_{CMB} = 2.73\,\mathrm{K}$.

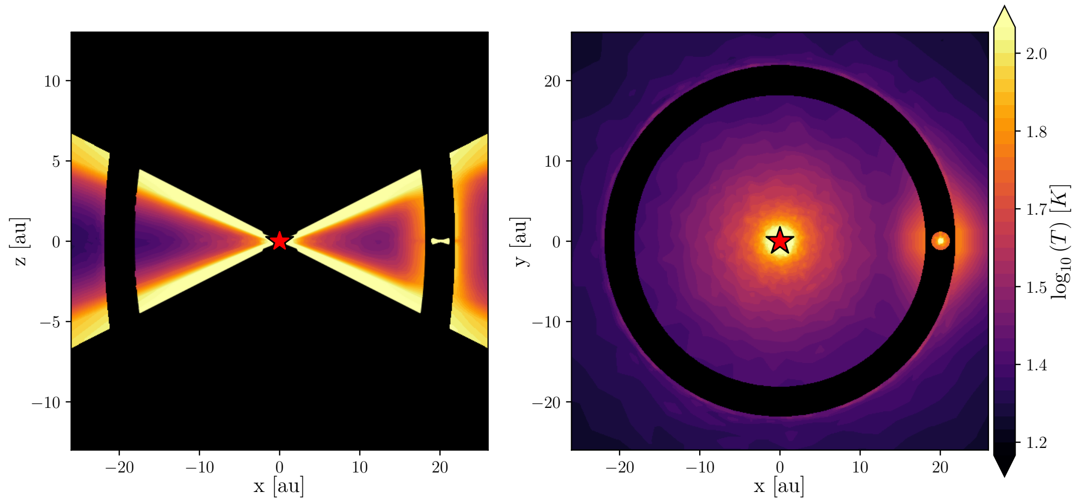

Figure 3.7: The xz-plane (*left*) and midplane cut (*right*) of the 3D temperature structure for a default planet luminosity ($L_p = 1.01 \times 10^{-2}\,\mathrm{L}_\odot$). Note that the temperature (i.e., the colorbar) is logarithmically scaled.

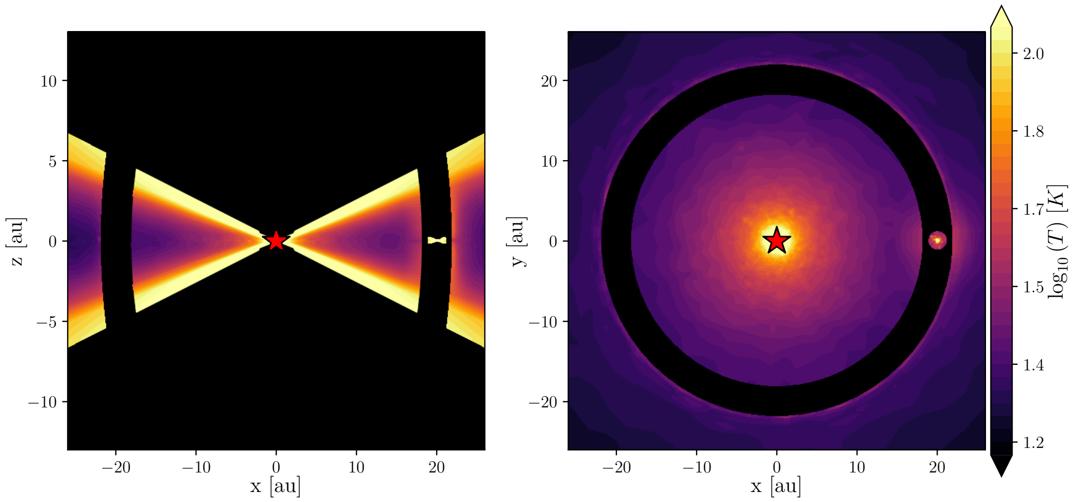

Figure 3.8: Exact same set-up as shown above, but now the planet luminosity has been reduced by an order of a magnitude — $L_p = 1.01 \times 10^{-3}\,\mathrm{L}_\odot$.

By considering the radius in the midplane cut ($y = 0$ and $z = 0$, only x varies), the temperature profile as function of radius that goes through all three zones is obtained (Fig. 3.9). The inner disk (green) starts at $x = 0.4$ au with a temperature of ~ 623 K which, at first, slowly declines as function of x (note how the temperatures values cluster at $x \approx 0.4$ au) until it starts to decline exponentially till at around 0.5 au. At that point the shallow slope indicates a linear (in log-log space) and smooth decline; the star's radiation has become mostly extinct and thus the dust grains heat each other via thermal emission only. Notice how the temperature of the last few data points slightly increases as it approaches the CPD. The zoomed-in plot in the top left corner depicts how the temperature of the outer edge of the inner disk (~ 54 K, at 18 au) is almost equal to the first data point of the left side of the CPD (CPDL, ~ 52 K). The temperature then shoots up as it approaches the planet with a maximum temperature of $T_{\mathrm{max}} = 2263$ K which is somewhat cooler than the planet ($T_p = 2500$ K). As it enters the right side of the CPD (CPDR) and moves away from the planet, the temperature decreases until it is roughly the same as the inner edge of the outer disk (~ 55 K). The temperature of the outer disk then decreases linearly as it moves away from the planet and starts approaching $T_{\mathrm{CMB}} = 2.73$ K. The lack of data points between the CPD and the surrounding disks represents the gap in which the CPD has been placed.

In Fig. 3.10 the same plot is shown for the lower planet luminosity $L_p = 1.01 \times 10^{-3}\,\mathrm{L}_\odot$. The behaviour of the the CPD is still the same, except for the grid points centered around $x = 20$ au; no photons have reached those areas and are thus equal to T_{CMB}. The values on the y-axis have also declined as the maximum temperature is now equal to ~ 1717 K.

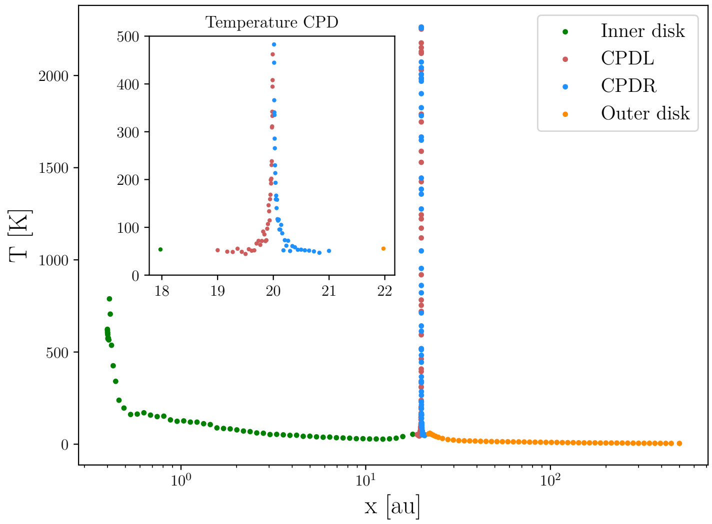

Figure 3.9: Temperature in the midplane along the line of the star and planet as function of x ($L_p = 1.01 \times 10^{-2}\,\mathrm{L}_\odot$). The colours green, red, blue and orange represent the inner disk, CPDL, CPDR and outer disk, respectively. The panel on the top left is a zoom-in of the CPD in which the green and orange dot represent the the last and first data point of the inner and outer disk, respectively. The y-axis has been capped at $T = 500\,\mathrm{K}$ so that the exponential curve in temperature of the CPD close the planet can be clearly discerned.

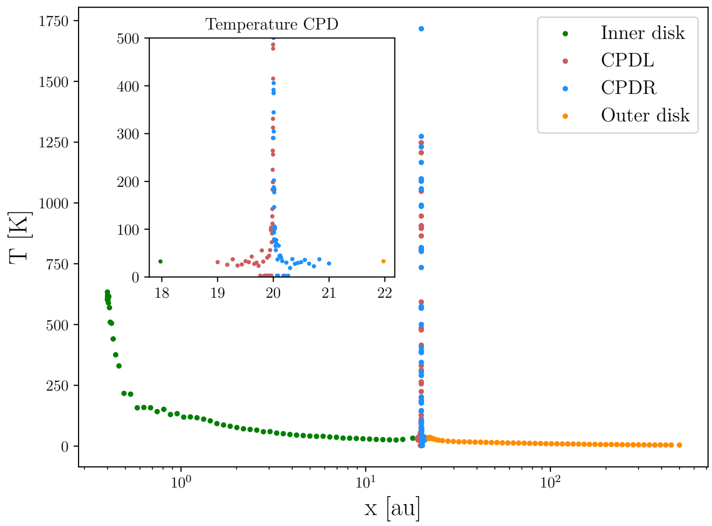

Figure 3.10: Temperature in the midplane for the lower luminosity case ($L_p = 1.01 \times 10^{-3}\,\mathrm{L}_\odot$).

In order to gain more insight on the influence of the CPD on the inner and outer disk, we ran the exact same model only without the CPD and the planet. We then compared the two models in Fig. 3.11 by plotting the resulting inner and outer disk together.

The blue and orange lines showcase the behaviour of the inner and outer disk with a CPD in between them. Conversely, the green and red are the inner and outer disk *without* a CPD or planet placed in between them. Notice how the blue line traces the green line, apart from the MC noise, closely until it starts moving upwards at $x \approx 10\,\mathrm{au}$. The blue line's temperature keeps increasing up till $\sim 54\,\mathrm{K}$ at which point it has reached the outer edge of the inner disk ($x = 18\,\mathrm{au}$). The difference in temperature of the blue and green line is at that point $\sim 31\,\mathrm{K}$. At $x = 22\,\mathrm{au}$ the photons hit the inner edge of the outer disk. However, now both the outer disk with and without the CPD shoot up in temperature (their temperature difference is now $\sim 27\,\mathrm{K}$); the outer disk is clearly heated up by the CPD, but what about the outer disk that has no CPD near it? Due to the gap, the stellar photons can actually hit the inner rim of the outer disk. And because of flaring, the inner rim of the outer disk is larger along z than the outer rim of the inner disk (e.g., left panel Fig. 3.8), resulting in a larger surface area for the stellar photons to impinge on. As a consequence, the inner rim of the outer disk will be additionally heated by the star.

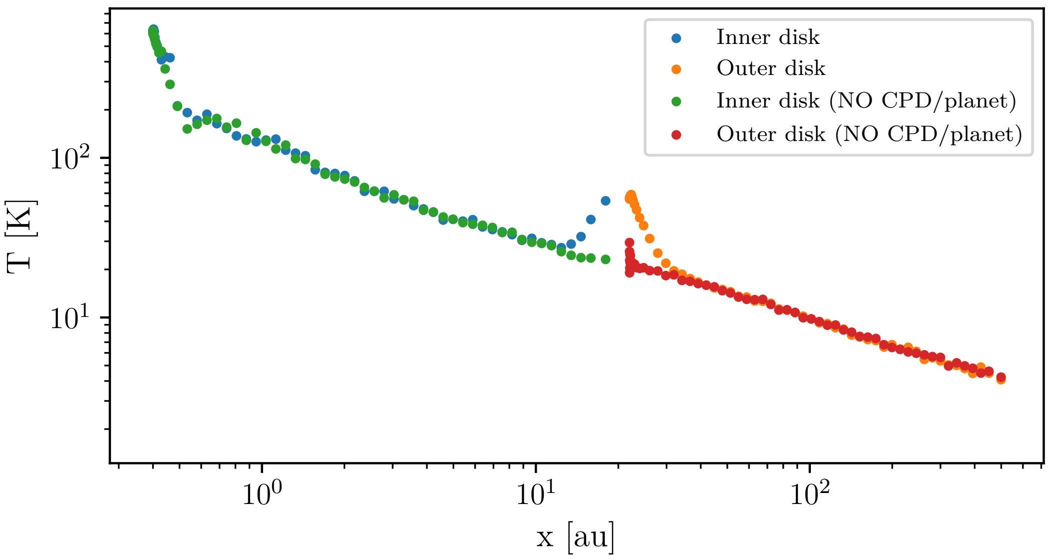

Figure 3.11: Midplane temperature as function of radius for inner and outer disk for $L_p = 1.01 \times 10^{-2}\,\mathrm{L}_\odot$.

Now, in order to properly compare the temperature of the outer edge of CPDL with that of CPDR, the Monte Carlo noise ought to be reduced like we did in Sect. 3.1.1. The true aim of this procedure is to obtain a reliable comparison between CPDL and CPDR. Fig. 3.12 and Fig. 3.13 display the the temperature for both CPDL and CPDR as function of radial grid points for the $L_p = 1.01 \times 10^{-2}\,\mathrm{L}_\odot$ and $L_p = 1.01 \times 10^{-3}\,\mathrm{L}_\odot$, respectively. The yellow (left) and green (right) plots are all the temperatures for the relevant ϕ-values which have been overplotted with its average temperature (blue and black line) and its additional error bars (for a more thorough explanation see Fig. 3.1 and Fig. 3.2).

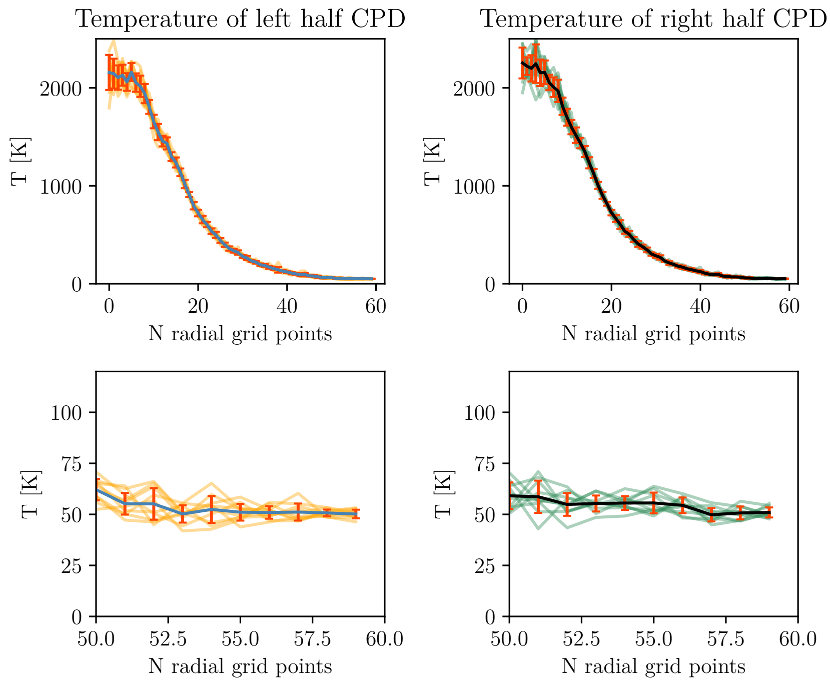

Figure 3.12: Radial temperature profile as function of radial grid points in the midplane for the sextant of ϕ-values for $L_p = 1.01 \times 10^{-2}\,\mathrm{L}_\odot$.

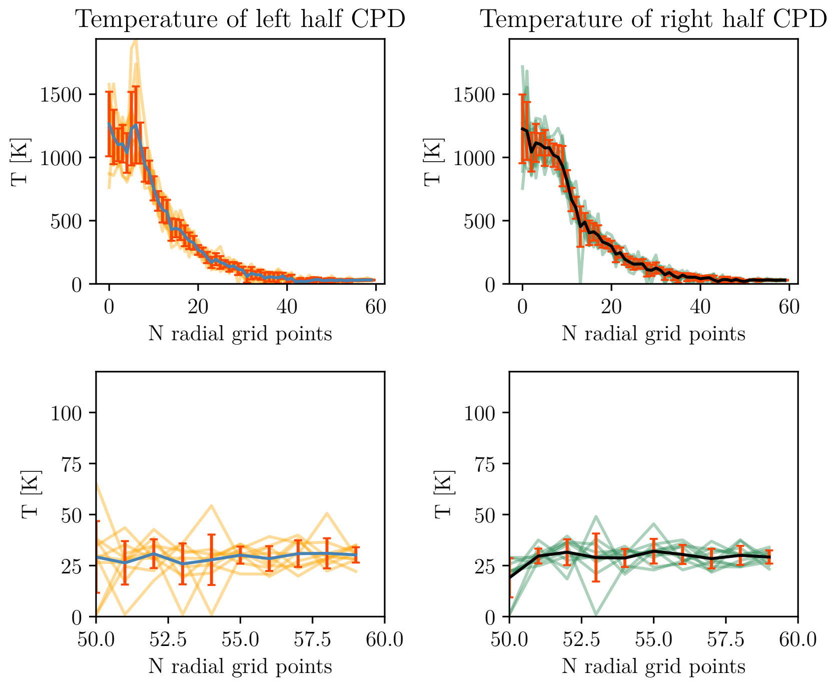

Figure 3.13: Radial temperature profile as function of radial grid points in the midplane for the sextant of ϕ-values for $L_p = 1.01 \times 10^{-3}\,\mathrm{L}_\odot$

By plotting the average temperatures obtained in Fig. 3.12 and Fig. 3.13 together as function of distance to the planet, a more detailed comparison can be realized. In Fig. 3.14 the temperature is plotted as function of CPD radius ($|x|$) on logarithmic scales. In the top plot one can see how the temperature first declines exponentially in log-log space (at around 3×10^{-3} au) and then continues to decline linearly in log-log space due to the self-heating of the dust.

In bottom panel of Fig. 3.14 the last three data points close to the CPD's edge are shown. The last data points of CPDL and CPDR at $x = 1$ au (i.e. the outer rim) have a value of $T_{CPDL} = (50 \pm 2)$ K and $T_{CPDR} = (51 \pm 3)$ K, respectively. Notice how CDPL is slightly lower in temperature than CDPR, which is the opposite of what we expected. However, since their difference is minute and their errors clearly overlap, we conclude that CPDL and CPDR must be equal in temperature. For the lower luminosity case (Fig. 3.15; top panel), the exponential decline on log-log scale is very similar to the standard luminosity case (Fig. 3.14). But for increasing x-values, the temperature starts to become more noisy as their uncertainties start to increase. As for the bottom panel, we can draw a similar conclusion as for L_p: the temperatures at the outer rim amount to $T_{CPDL} = (30 \pm 4)$ K and $T_{CPDR} = (29 \pm 3)$ K, i.e. CPDL is again equal to CPDR.

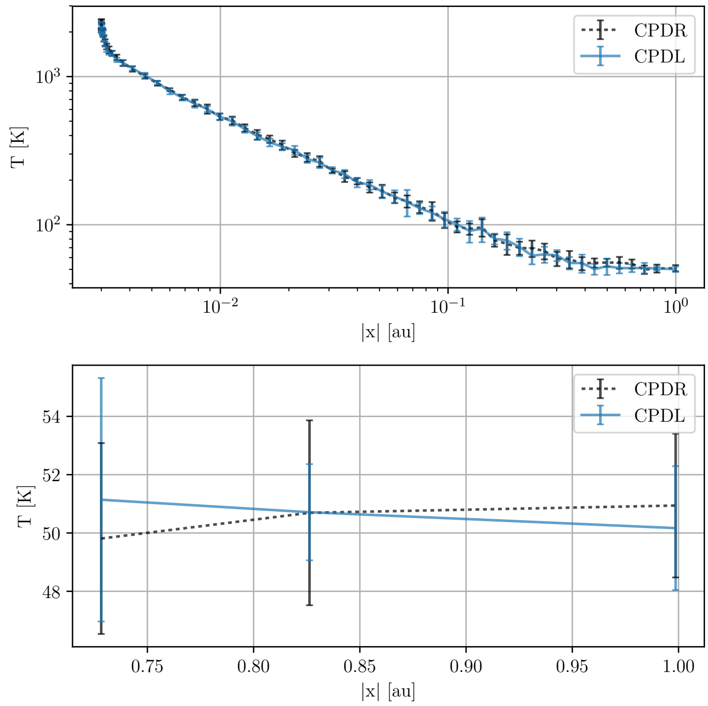

Figure 3.14: The average temperatures of CPDL and CPDR including their errors for $L_p = 1.01 \times 10^{-2}\,L_\odot$ as function of distance to the planet. *Top:* CPDR and CPDL plotted on a logarithmic scale. *Bottom:* zoom-in of the last three data points plotted on a linear scale.

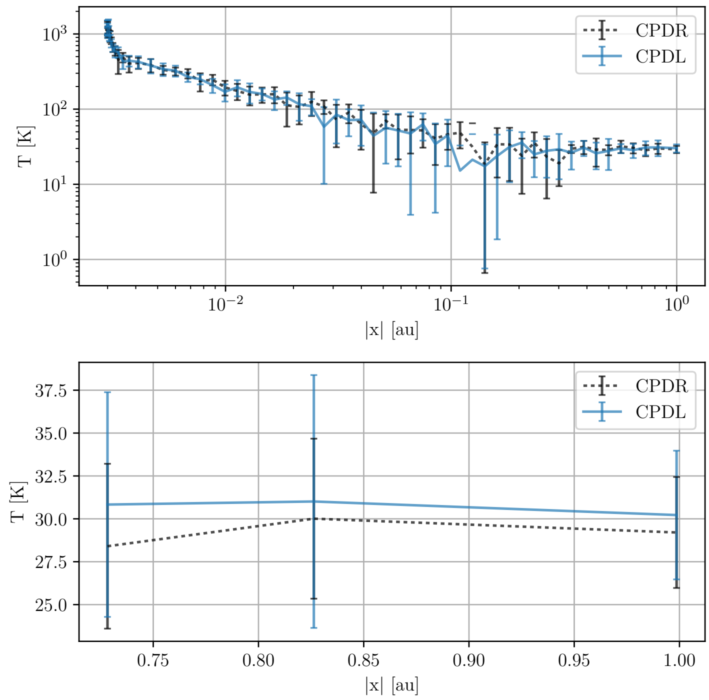

Figure 3.15: Same as Fig. 3.14 but for a lower planetary luminosity ($L_p = 1.01 \times 10^{-3}\,\mathrm{L}_\odot$).

3.3.2 Radiation field

For the radiation field we focus on the wavelength range of $0.091\,\mu\mathrm{m} < \lambda < 0.205\,\mu\mathrm{m}$ which comprises the Far-UV spectrum. This wavelength range plays an important role in the chemistry of the CPD (e.g., photo-ionization and photo-desorption processes). The radiation field is normalized to the *Draine field*, which is a unitless quantity and is equal to 1 for the interstellar radiation field (B. T. Draine and Bertoldi 1996; Woitke, Kamp, et al. 2009). This means that a radiation field of 10^6, for example, is 10^6 times stronger than the interstellar radiation field.

The radiation field is computed separately from the temperature by using its own predefined set of photons. MCMax3D uses a total of 3×10^6 photons, which it distributes and subsequently integrates over 21 wavelengths points that comprise the $0.091\,\mu\mathrm{m} < \lambda < 0.205\,\mu\mathrm{m}$ wavelength range.

The results for the radiation field in the xz-plane exhibited quite a few voids, i.e. some grid points did not receive any radiation field photons. In fact, the radiation field was noisier than the temperature. In order reduce the Monte Carlo noise as much as possible, we averaged over *all* the ϕ-values for the θ-values that constitute the upper hemisphere of the CPD (the lower hemisphere can be neglected, as the radiation field is symmetric around the midplane). The procedure is similar the one shown in Fig. 3.1, but now the ϕ-values map out the entire circle instead of two sextants.

The result for the default luminosity is depicted in Fig. 3.16: the isotropic nature of the radiation and the averaging procedure are responsible for the symmetry along z at $x = 20\,\mathrm{au}$ ($\theta = 0$) and the well-stratified nature of the annuli. As with the flux, the radiation field decreases as function of $1/r^2$. The lack of data points at $\theta = 0$ is due to a limitation of the code. Notice how the annular structure disappears in the midplane ($z = 0$); the greater optical depth makes it more difficult for the photons to penetrate, which weakens the radiation field's intensity (as evidenced by the darker patches). Do not be fooled by the seemingly smooth structure of the contour plot, however; there are actually very few data points, but the empty spaces are filled up by plotting routine. This leads to a wrong impression of the actual accuracy of the radiation field.Because of these inaccurate results, we decided to only show the default luminosity case ($L_p = 1.01 \times 10^{-2}\,\mathrm{L}_\odot$) as lowering the luminosity would only lead to even worse results.

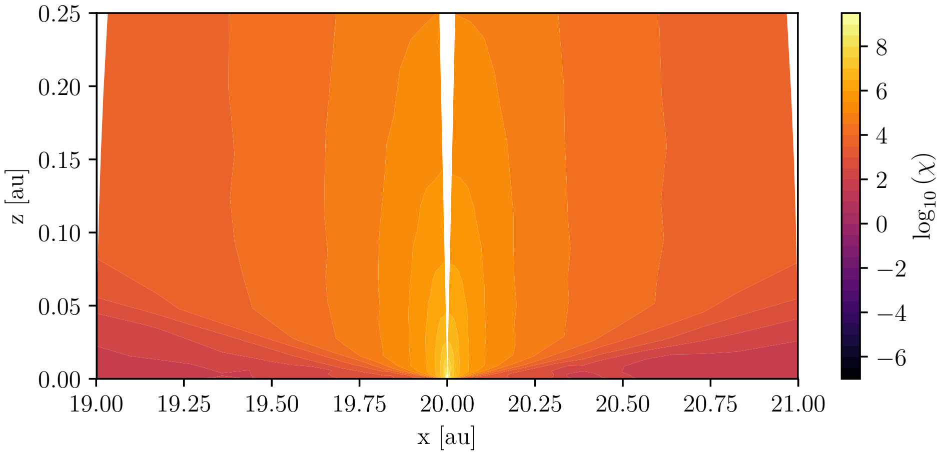

Figure 3.16: xz-plane of the average radiation field for $L_p = 1.01 \times 10^{-2}\,\mathrm{L}_\odot$.

The outer rim of CPDL (just like with the temperature) might have a stronger radiation field than the outer rim of CPDR if the intensity of the stellar radiation is strong enough. Following the same methodology as for Fig. 3.12 and as describe in Sect. 3.1.1, we can plot the average radiation field in the midplane as function of radial grid points. In Fig. 3.17, the first thing that strikes the eye, is the asymmetry of the errors. This is because the radiation field, χ, has been plotted on a log-scale. Moreover, the errors are so large that they extend all the way to about $\sim -10^9$, and we only plotted for positive χ-values (as negative values are non-physical). The reason for these massive errors has to do with the fact that a lot of grid points have undefined values for the radiation field (set at $\chi = 0$), as they were never hit by a photon. If we then average over the ϕ-values for each radial grid point along CPDL or CPDR, we get a very inaccurate average value and thus extremely large standard deviations.

Close to the planet, the radiation field starts with a value of about 10^9 (for both CPDL and CPDR) which decreases as function of radial grid points. Both CPDL and CPDR abruptly drop off to $\chi = 0$ after which they climb up again until they reach a local maximum of roughly $\chi = 10^4$ after which they decline again until they settle at about $\chi = 10^2$.

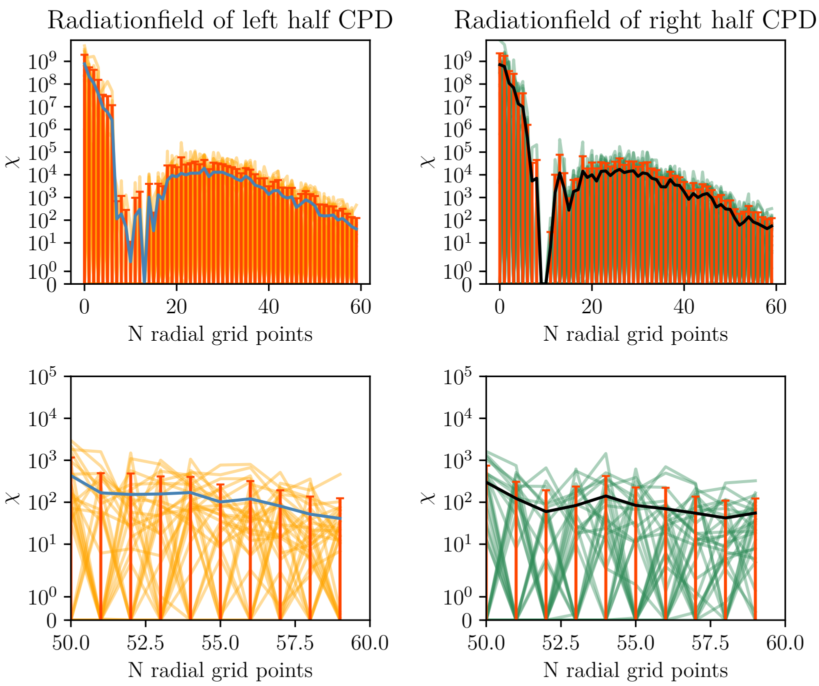

Figure 3.17: Radiation field (χ) in midplane as function of radial grid points for all ϕ-values ($L_p = 1.01 \times 10^{-2}\,\mathrm{L}_\odot$). The radiation field is plotted on a logarithmic scale and the radial grid points on a linear scale. The yellow and green lines are the radiation fields plotted for all ϕ-values, the overplotted blue and black line represent the average radiation field for CPDL and CPDR, respectively. The orange-red error bars below the average are so stretched out due the logarithmic scaling. Notice the zero values of χ at $nr = 12$ for CPDL and $nr = 8, 9$ for CPDR.

Finally, by plotting the average radiation field of CPDL and CPDR together, we can visualize and infer the star's influence on the CPD (as done before in Fig. 3.14). In Fig. 3.18, the radiation field is plotted as function of CPD radius ($|x|$) on logarithmic scales. In the bottom plot, a zoom-in of the last three data points highlights the difference between CPDL and CPDR at the outer rim. At $x = 1\,\mathrm{au}$ their values amount to $\chi_{CPDL} = 41 \pm 83$ and $\chi_{CPDR} = 55 \pm 68$. Their overlapping errors prove that they are equivalent (as also evident from the plot).

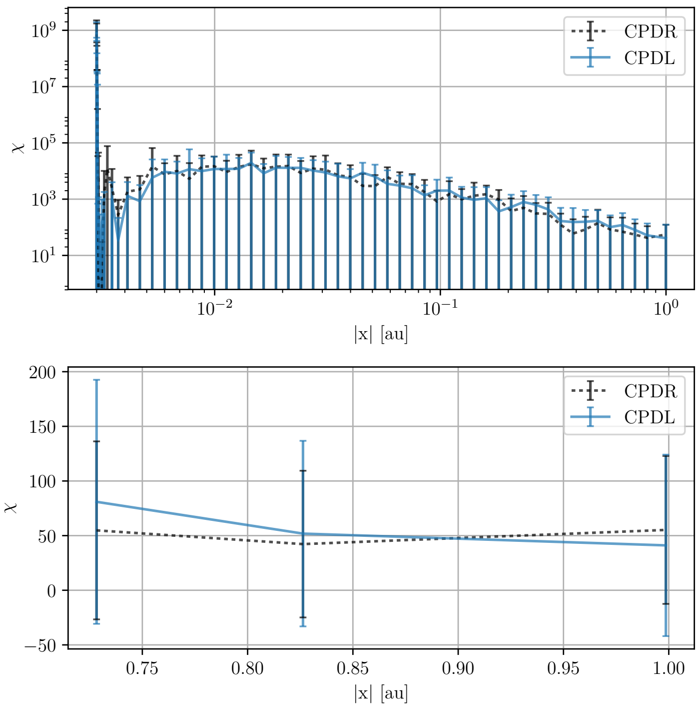

Figure 3.18: The average radiation field of CPDL and CPDR with their errors as function of distance to the planet for $L_p = 1.01 \times 10^{-2}\,\mathrm{L}_\odot$. The x-values for both plots have been adjusted such that the planet is located at $x = 0\,\mathrm{au}$ for both cases. *Top:* CPDR and CPDL plotted on a logarithmic scale. The bottom errors appear stretched due to the logarithmic y-axis. *Bottom:* zoom-in of the last three data points plotted on a linear scale.

3.4 Configuration 2: No inner disk

3.4.1 Temperature

The first noticeable difference — for both planet luminosities — after removing the inner disk, is how the star now irradiates the outer disk directly. The stellar radiation is so strong, that planet/CPD emission onto the inner rim of the outer disk has become negligible (See left panel Fig. 3.19). Furthermore, the left side of the CPD for the low luminosity case (Fig. 3.20) seems to be hotter than the right side, implying that the star heats it up additionally.

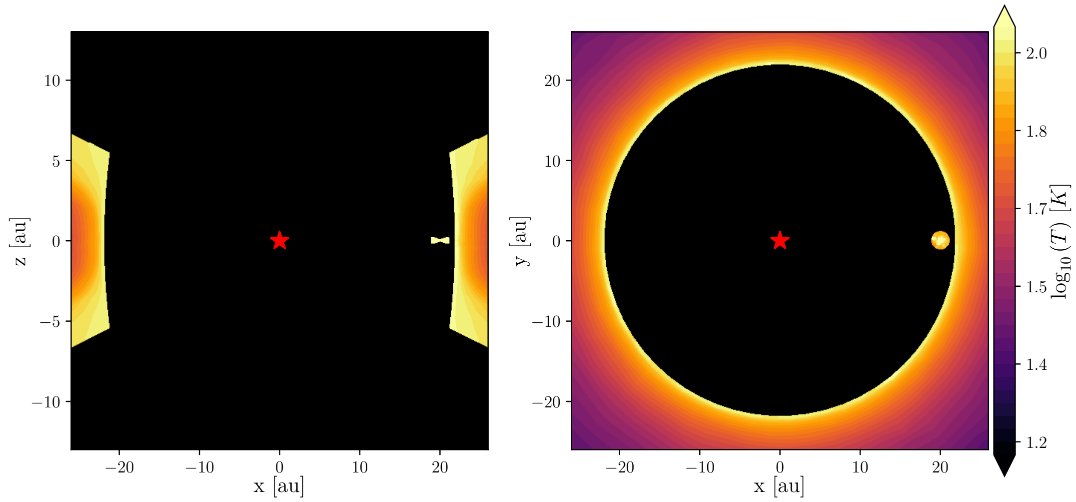

Figure 3.19: The xz-plane (*left*) and midplane cut (*right*) of the 3D temperature structure for the default planet luminosity ($L_p = 1.01 \times 10^{-2}\,\mathrm{L}_\odot$).

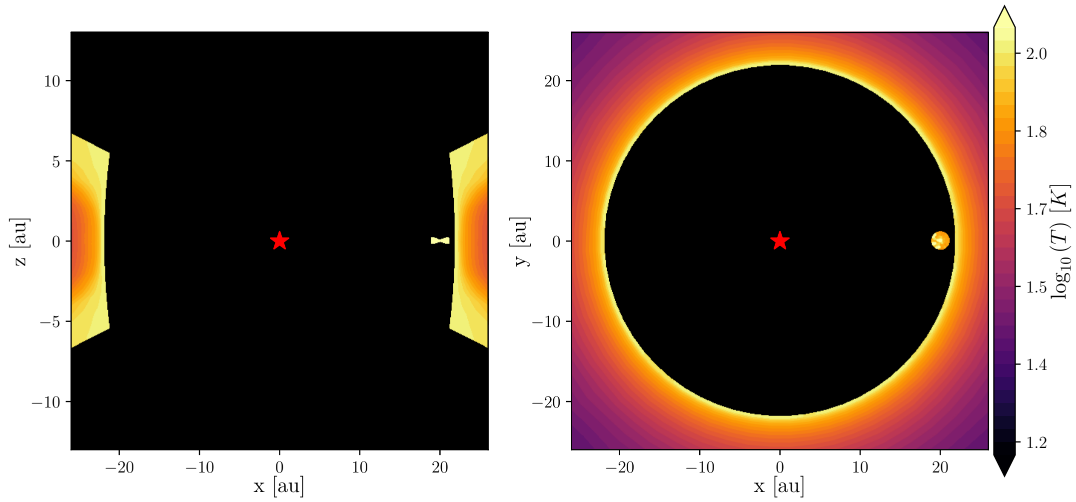

Figure 3.20: Exact same set-up as shown in Fig. 3.19, but now the planet luminosity has been reduced by an order of a magnitude — $L_p = 1.01 \times 10^{-3}\,\mathrm{L}_\odot$.

The radial temperature profile as function of radial grid points plots are omitted here, as they are not markedly different from the ones in the previous configuration. Furthermore, Their main purpose was to illustrate the averaging procedure to begin with (the same applies for the radiation field).

The average temperatures plots of CPDL and CPDR, however, are of interest: In Fig. 3.21, one can see how the temperature at the outer edge of CPDL is lower than that of CPDR, i.e. $T_{CPDL} = (58 \pm 6)\,\mathrm{K}$ and $T_{CPDR} = (68 \pm 6)\,\mathrm{K}$. This is opposite from what we expected, but the sudden temperature jump between the second to last and last data point indicate that Monte Carlo noise must be at play here. Conversely, in the lower luminosity case (Fig. 3.22) one can see an actual trend occur, meaning that the outer rim of CPDL does in fact get heated by the star, with temperature values at the outer rim of: $T_{CPDL} = (74 \pm 13)\,\mathrm{K}$ and $T_{CPDR} = (65 \pm 1)\,\mathrm{K}$. However, the errors overlap which implies that CPDL and CPDR are equal. Notice how the errors in CPDL are markedly larger than CPDR; a consequence from the star only heating up a few grid points on the left side of the CPD, which generates larger errors.

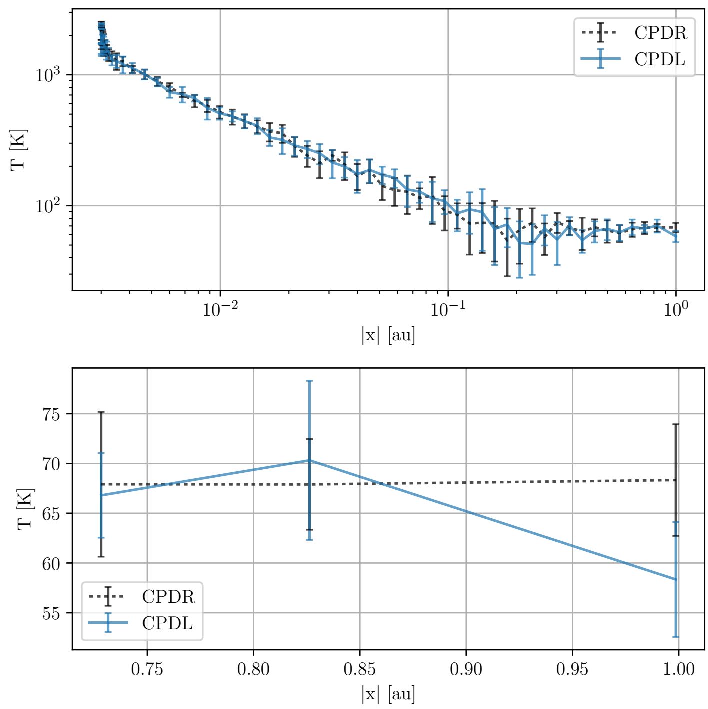

Figure 3.21: The average temperatures of CPDL and CPDR including their errors for $L_p = 1.01 \times 10^{-2}\,\mathrm{L}_\odot$ as function of distance to the planet. *Top:* CPDR and CPDL plotted on a logarithmic scale. *Bottom:* zoom-in of the last three data points plotted on a linear scale.

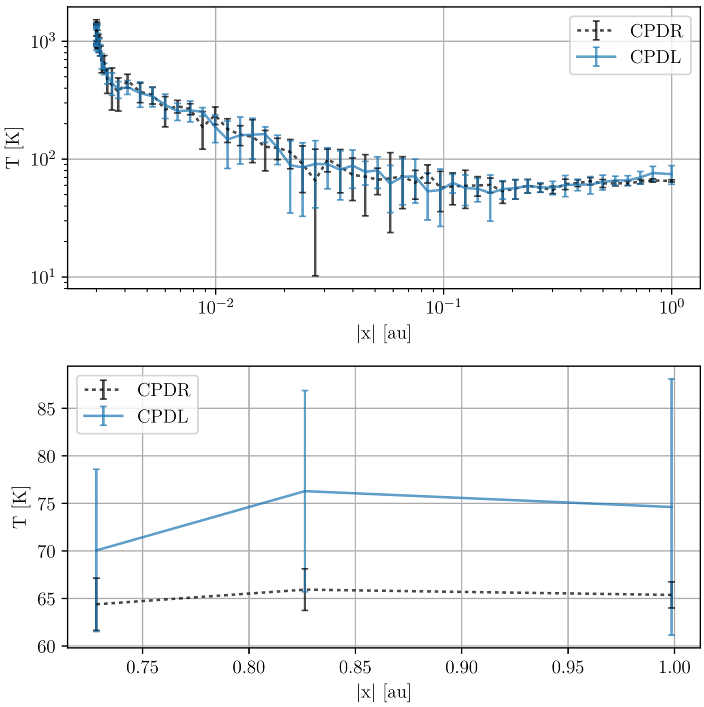

Figure 3.22: The average temperatures of CPDL and CPDR including their errors for $L_p = 1.01 \times 10^{-3}\,\mathrm{L}_\odot$. Notice how CPDL is consistently higher.

3.4.2 Radiation field

The removal of the inner disk, seemed to have diminished the isotropy of the CPD's radiation field (Fig. 3.23). More importantly, in Fig. 3.24 a trend starts to form in which the radiation field of CPDL is stronger than CPDR, with values at the outer rim of: $\chi_{CPDL} = (1 \pm 5) \times 10^4$ and $\chi_{CPDR} = 552 \pm 546$. The huge errors are again evidence of the inaccuracy of the radiation field.

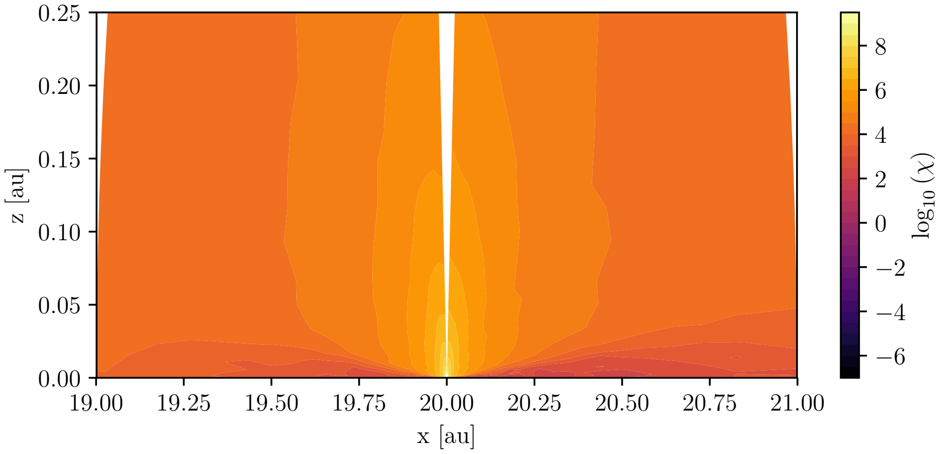

Figure 3.23: xz-plane of the average radiation field for $L_p = 1.01 \times 10^{-2}\,\mathrm{L}_{\odot}$.

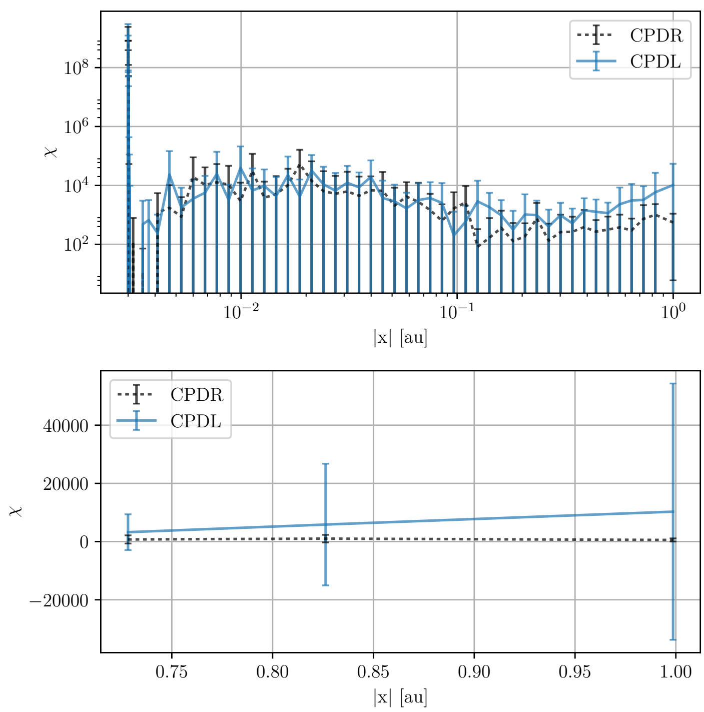

Figure 3.24: The average radiation field of CPDL and CPDR with their errors as function of distance to the planet for $L_p = 1.01 \times 10^{-2}\,\mathrm{L}_{\odot}$.

3.5 Configuration 3: No inner disk and closer to star

3.5.1 Temperature

In both Fig. 3.25 and Fig. 3.26, we notice an asymmetric temperature structure for the CPD and an outer disk that is clearly only heated by the star. Less noticeable — hardly noticeable, in fact — is the 'shadow' produced by the CPD. The inner edge of the outer disk is traced by a yellowish line, which is not present at the ϕ-values where the CPD is blocking the stellar radiation.

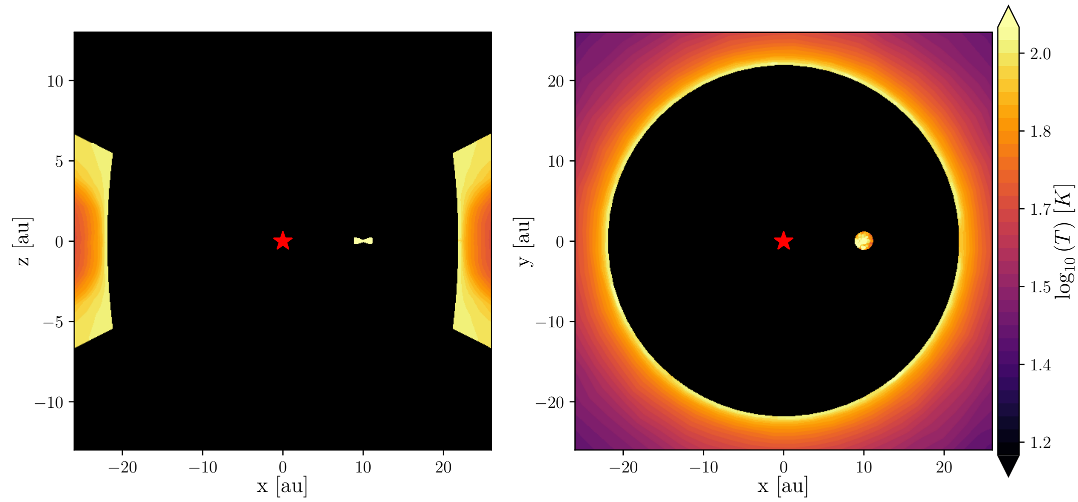

Figure 3.25: The xz-plane (*left*) and midplane cut (*right*) of the 3D temperature structure for a default planet luminosity ($L_p = 1.01 \times 10^{-2}\,L_\odot$).

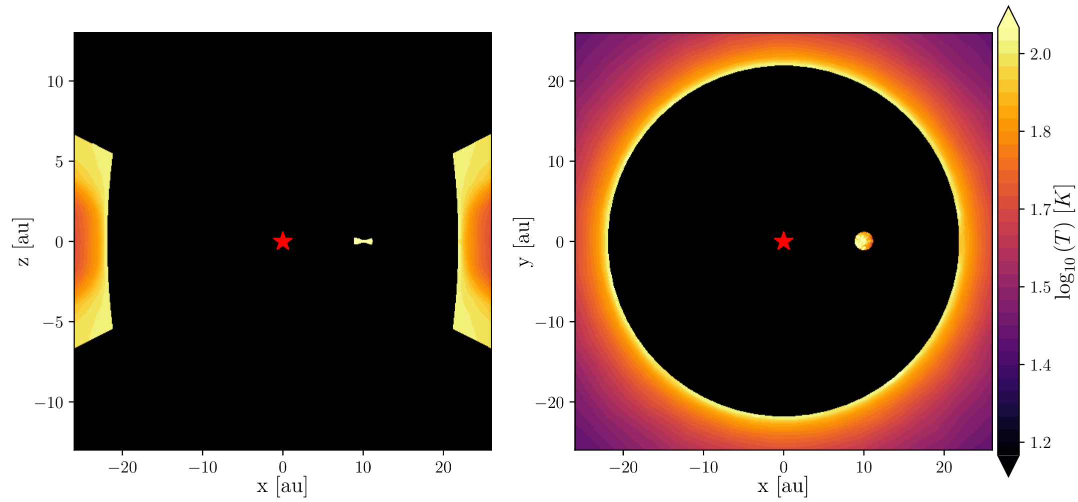

Figure 3.26: Exact same set-up as shown in Fig. 3.25, but now the planet luminosity has been reduced by an order of a magnitude — $L_p = 1.01 \times 10^{-3}\,L_\odot$.

Because the CPD is clearly heated by the star now, the radial temperature profile plots as function of radial grid points are now markedly different: In Fig. 3.27, one can see how the temperature of CPDL is clearly higher than CPDR. In Fig. 3.28, CPDR even seems to decline for the last few grid points, but that could also be due to Monte Carlo noise.

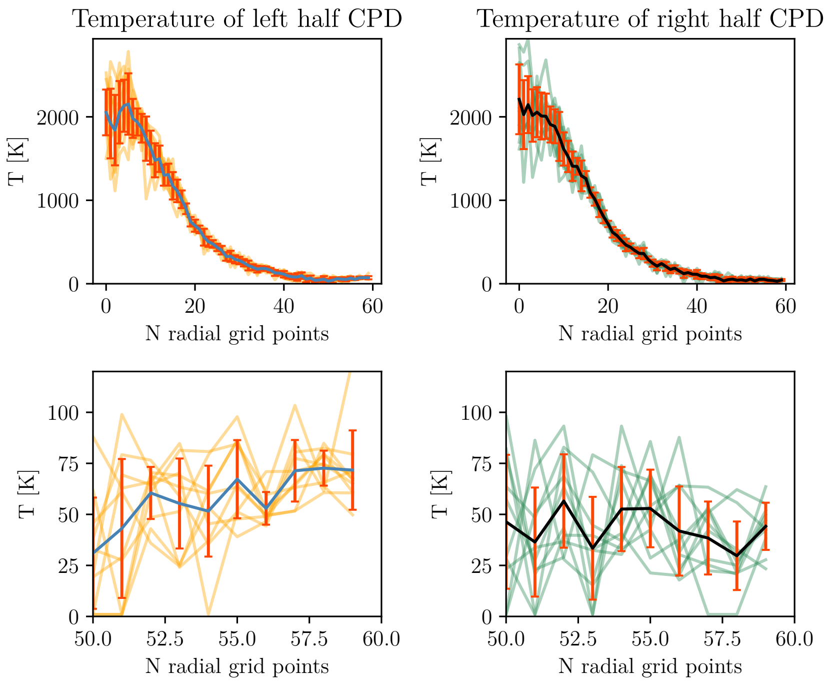

Figure 3.27: Radial temperature profile as function of radial grid points in the midplane for the sextant of ϕ-values for $L_p = 1.01 \times 10^{-2}\,\mathrm{L}_{\odot}$.

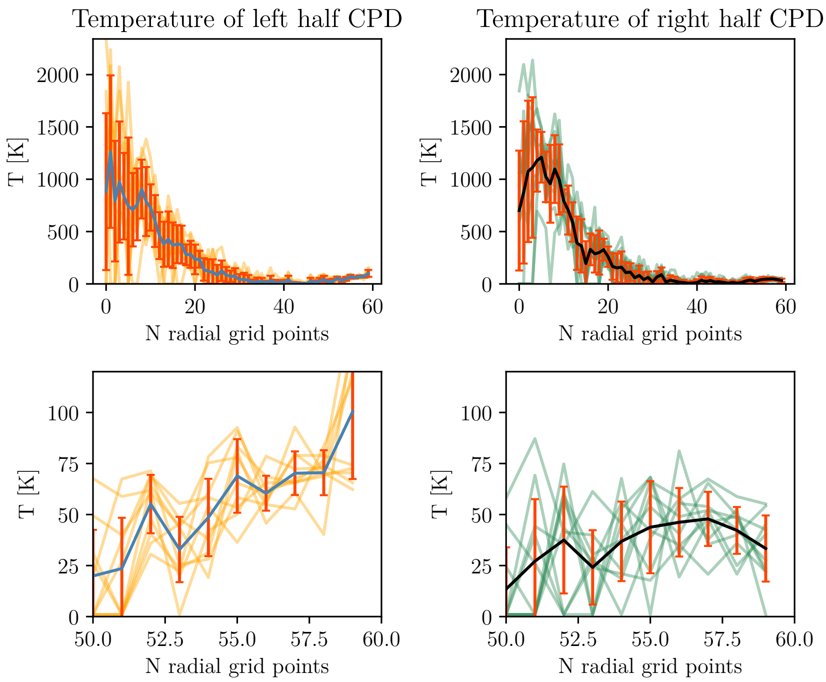

Figure 3.28: Radial temperature profile as function of radial grid points in the midplane for the sextant of ϕ-values for $L_p = 1.01 \times 10^{-3}\,\mathrm{L}_{\odot}$

By plotting CPDL and CPDR together we can see clear trends for both the default and low luminosity case (Fig. 3.29 and Fig. 3.30, respectively), with temperatures at the outer rim of: $T_{CPDL} = (72 \pm 20)\,\mathrm{K}$ and $T_{CPDR} = (44 \pm 12)\,\mathrm{K}$, for the default luminosity case, and $T_{CPDL} = (100 \pm 34)\,\mathrm{K}$ and $T_{CPDR} = (33 \pm 17)\,\mathrm{K}$, for the low luminosity case. Notice how in Fig. 3.30 the errors do not overlap for the last two grid points and that CPDR actually seems to decrease in temperature.

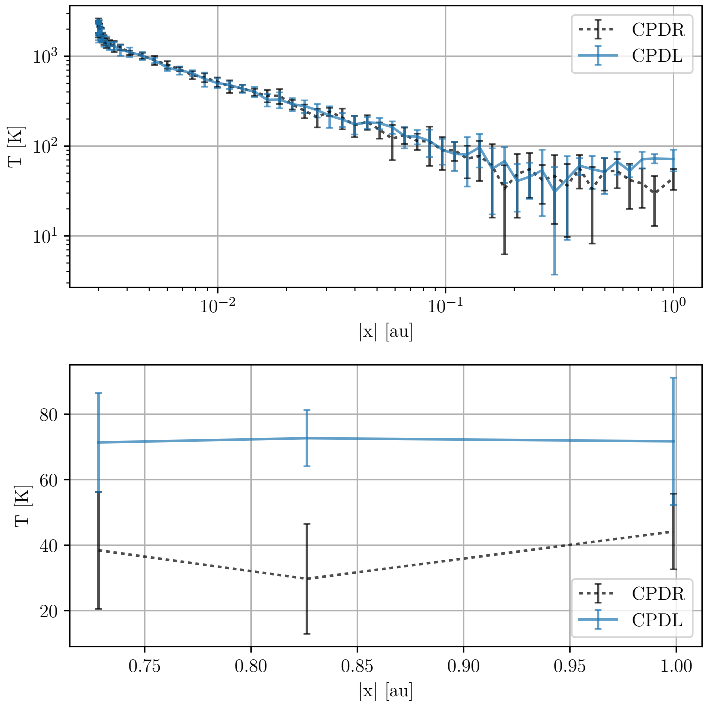

Figure 3.29: The average temperatures of CPDL and CPDR including their errors for $L_p = 1.01 \times 10^{-2}\,\mathrm{L}_{\odot}$ as function of distance to the planet. *Top:* CPDR and CPDL plotted on a logarithmic scale. *Bottom:* zoom-in of the last three data points plotted on a linear scale. *top:* one can distinguish a steep temperature fall-off between (3×10^{-2} au and 3.5×10^{-2} au), for larger radii the decline mellows down and becomes more shallow.

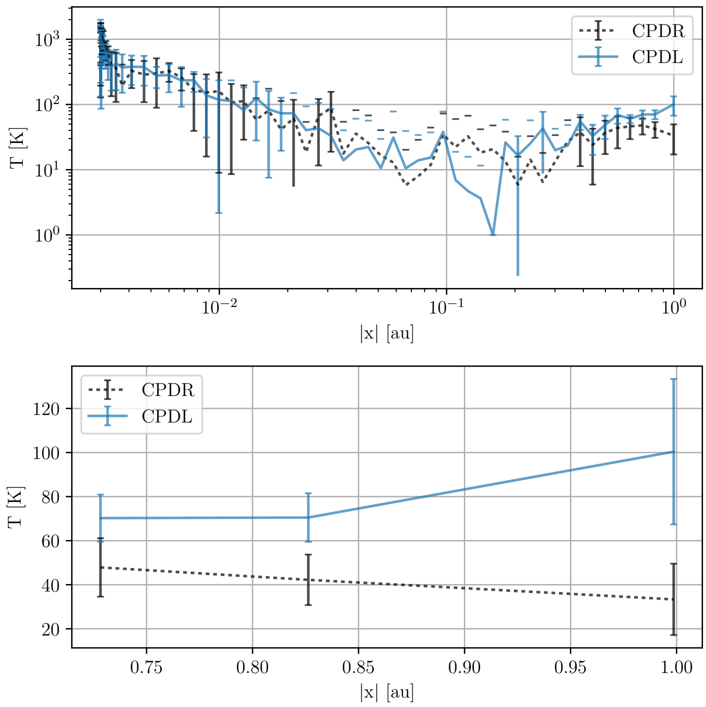

Figure 3.30: The average temperatures of CPDL and CPDR including their errors for $L_p = 1.01 \times 10^{-3}\,\mathrm{L}_{\odot}$.

3.5.2 Radiation field

Fig. 3.31 depicts the radial radiation field profile as function of radial grid points. Also note how the errors at the left side of the CPD at around 55th radial grid point are suddenly a lot smaller than the rest (the same can be seen in CPDL at the 58th radial grid point). This is simply because at those points the values of the radiation field are quite equal, i.e. most of the ϕ-values at those radial grid points have an actual radiation field value. Finally, in Fig. 3.32 the errors of CPDL are markedly larger than CPDR; a consequence of the star only irradiating random areas on the left of the CPD. The values of CPDL and CPDR at the outer rim amount to: $\chi_{CPDL} = (2.5 \pm 0.4) \times 10^4$ and $\chi_{CPDR} = (4.7 \pm 0.9) \times 10^3$.

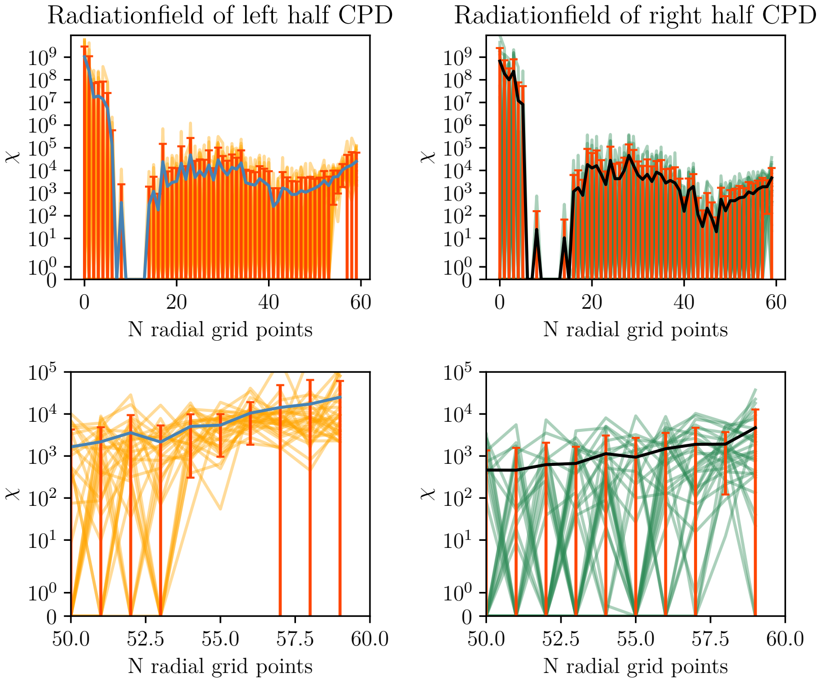

Figure 3.31: Radiation field (χ) in midplane as function of radial grid points for all ϕ-values ($L_p = 1.01 \times 10^{-2}\,\mathrm{L}_{\odot}$).

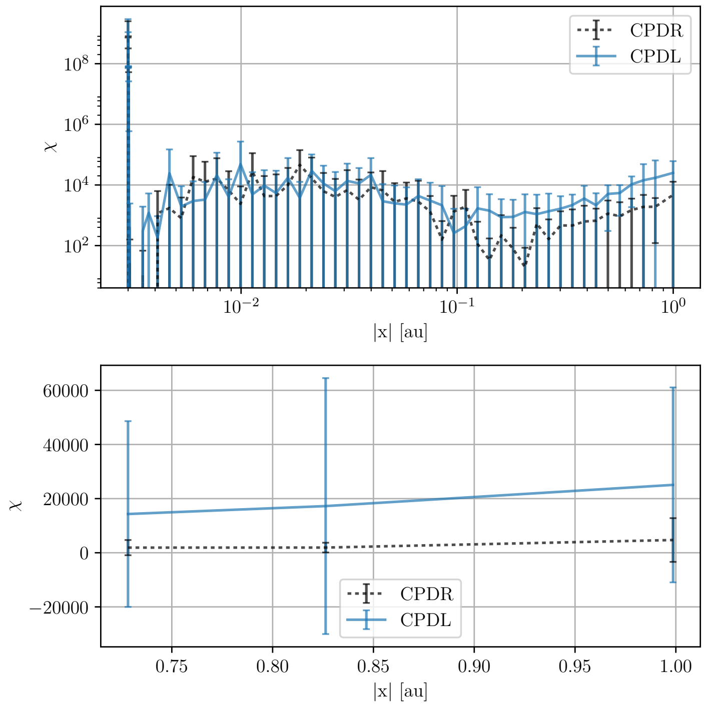

Figure 3.32: The average radiation field of CPDL and CPDR with their errors as function of distance to the planet for $L_p = 1.01 \times 10^{-2}\,\mathrm{L}_{\odot}$.

Chapter 4

Discussion and conclusion

> Something is wrong... Don't worry! I'll try to fix it.
>
> *MCMax3D*

For this project we tested how the temperature and radiation field in a static circumplanetary disk (CPD) model changes due to irradiation from its host star. And what environmental circumstances would increase or decrease the influence of the star's irradiation onto the CPD. Additionally, we also had a short look at the CPD's impact on the temperature of its surroundings, i.e. the protoplanetary disk (PPD) in which it resides.

We used MCMax3D to build up a protoplanetary disk consisting of an inner disk and an outer disk. These disks were separated by a gap in which a planet with a surrounding CPD was placed at a 20 au distance from the star. For a total of 6 models — each using 10^9 photon packages and a grid point configuration of $(\phi, \theta, r) = (60, 50, 60)$ abbreviated as HL — we tested the influence of the star on the temperature and radiation field of the CPD. From the geometry of our set-up we argued that the outer rim of CPDL (side of the CPD that is pointing in the direction of the star) would be hotter than the outer rim of CPDR (side that is pointing away from the star). The CPD itself was left unchanged for all models, meaning that its radius was always 1 au and thus the outer rim of CPDL was always 2 au closer to the star than the outer rim of CPDR. We distinguish three configurations:

1. the full system with inner disk, outer disk, and CPD placed in between them (HL).
2. the full system but inner disk removed (HLNODISK).
3. the full system but inner disk removed and planet and CPD placed at 10 au distance from the star (HLNODISK10au).

Each of these configurations were tested twice: one with the default planet luminosity $L_p = 1.01 \times 10^{-2}\,\mathrm{L}_\odot$ and one with the planet luminosity reduced by an order of magnitude $L_p = 1.01 \times 10^{-3}\,\mathrm{L}_\odot$ (the model will then have 'lumlow' attached to its abbreviation). In order to reduce the Monte Carlo noise, we averaged over a sextant of ϕ-values for CPDL (solar direction) and CPDR (anti-solar direction) for the temperature. Because radiation field was even more noisy, we averaged over the whole annulus of ϕ-values. The results of the temperature and radiation field at the outer rim of the CPD for the various models are displayed in Table 4.1. Note that we did not treat the radiation field for the lower luminosity case, as its values would only be worse. Their values are, however, listed in Table 4.1 for completeness.

Model	**Config.**	Temperature [K]		Radiation field	
		T_{CPDL}	T_{CPDR}	χ_{CPDL}	χ_{CPDR}
HL	1	50 ± 2	51 ± 3	41 ± 83	55 ± 68
HLlumlow	1	30 ± 4	29 ± 3	5 ± 10	7 ± 14
HLNODISK	2	58 ± 6	68 ± 6	$(1 \pm 5) \times 10^4$	552 ± 546
HLNODISKlumlow	2	74 ± 13	65 ± 1	$(8 \pm 20) \times 10^3$	$(1.3 \pm 2.0) \times 10^3$
HLNODISK10au	3	72 ± 20	44 ± 12	$(2.5 \pm 0.4) \times 10^4$	$(4.7 \pm 0.9) \times 10^3$
HLNODISK10aulumlow	3	100 ± 34	33 ± 17	$(7.2 \pm 2.0) \times 10^4$	$(2 \pm 3) \times 10^3$

Table 4.1: Values of the temperature and radiation field at the outer rim of CPDL (side facing the star) and CPDR (side facing away from the star) for all six models.

For configuration 1 we found that — for both the default and lowered planet luminosity — the star did not have any influence on the CPD's temperature and radiation field, i.e. the temperature gradient of the CPD remained symmetric. Because the CPD was surrounded by an inner and outer disk, we also investigated how the CPD influenced the inner and outer disk. We ran an additional HL model in which we removed the planet and CPD (but we retained the gap). We found that in the midplane aligned with the star and planet ($\phi = 0$ and $\phi = \pi$), that the last radial grid point of the inner disk's outer edge was an additional $\sim 31\,\mathrm{K}$ warmer due to the planet and CPD's irradiance. Similarly, the planet and CPD increased the temperature of the outer disk's inner edge with an additional $\sim 27\,\mathrm{K}$. The smaller difference in temperature for the outer disk was brought about by the gap separating the inner from the outer disk; stellar photons reached the inner edge of the outer disk via the gap as they got scattered towards the midplane from the surface layers.

In configuration 2 we found that, for the default planet luminosity ($L_p = 1.01 \times 10^{-2}\,\mathrm{L}_\odot$), the temperature at the outer rim did not change. For the lower luminosity ($L_p = 1.01 \times 10^{-3}\,\mathrm{L}_\odot$), however, the temperature for the last three data points of CPDL were all higher than CPDR. Unfortunately, their errors still overlapped, implying that there is no difference between the two. However, the fact that CPDL was consistently higher for the last three data points than CPDR did show us that a trend was forming. The same was true for the radiation field: for both default and the lower planet luminosity, we found that the temperature of CPDL was higher than CPDR for the last three data points, yet their errors still overlapped.

Finally, for the default luminosity in configuration 3, we found that the temperature of CPDL was consistently higher than CPDR for the last four data points, and that their errors in the second to last point did not even overlap (Fig. 3.29). However, for the very last data point (at $x = 1\,\mathrm{au}$) the temperature of CPDR suddenly increased again such that the errors overlapped again. But when we reduced the planet's luminosity to $L_p = 1.01 \times 10^{-3}\,\mathrm{L}_\odot$, we found that for the last two data points the temperature of CPDL was higher than CPDR and that their errors did not overlap either. What's more, as CPDL and CPDR approached their respective outer rim the temperature of CPDL *increased* while the temperature of CPDR *decreased* (Fig. 3.30).

For the set-up that we used (see Table 4.1, for the exact details), we thus found that the inner disk was too optically thick for the stellar radiation to penetrate and reach the CPD in the midplane; no difference in temperature structure was found for both planetary luminosities. When we removed that inner disk we noticed that the difference between CPDL and CPDR became more apparent, but due to their overlapping errors we could not conclude that the

difference was very significant, i.e. the Monte Carlo noise was still too great. However, when we removed the inner disk and reduced the distance between the star and the planet from 20 au to 10 au, we noticed a significant difference. This difference was even greater when the planet's luminosity was reduced to $L_p = 1.01 \times 10^{-3}\,\mathrm{L}_\odot$. The error of CPDL also increased when the stellar radiation was strong enough to heat it up. This had to due with the fact that only certain patches were heated up by the star, meaning that still too few stellar photons hit the left side of the CPD to sufficiently reduce the Monte Carlo noise. As for the radiation field, it followed the same trend as the temperature (i.e., how it changed for the 6 different models), but in all cases the Monte Carlo noise was too great for it to have any reliable results.
In short the stellar flux impinging on the CPD become stronger when:

1. there is no attenuating medium in between the the star and the CPD (i.e., an inner disk)
2. the CPD is closer to the star, so that it receives more stellar photons.
3. the planet's luminosity relative to the star's luminosity is lowered

4.1 Planet Vs Star

We can actually roughly quantify this difference in temperature and radiation field, by calculating the flux the outer rim of CPDL receives from the planet and the star (with the inner disk removed, of course; so only applicable for configuration 2 and 3). This procedure will be carried out for both planetary luminosities in only the midplane. Will also assume that both the star and planet are point sources. A schematic is shown in Fig. 4.1.

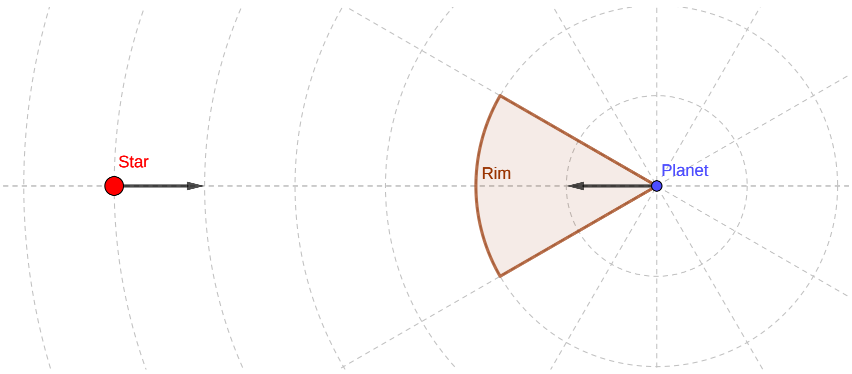

Figure 4.1: Schematic top-down view of star, planet and the left side of the CPD in midplane. Note that I erroneously placed the planet at the Origin. Please try to imagine that $x = 0$ au is the location of the star. *Scenario 1:* The star is located at $x = 0$ au, the planet at $x = 20$ au and the CPDL outer rim at $x = 19$ au. *Scenario 2:* The star is located at $x = 0$ au, the planet at $x = 10$ au and the CPDL outer rim at $x = 9$ au.

We consider two scenarios:

1. The star located at the Origin and the planet at $x = 20$ au
2. The star located at the Origin and the planet at $x = 10$ au

The flux is given to be (LeBlanc 2010):

$$F = \frac{L}{4\pi D^2} \tag{4.1}$$

where L is the luminosity in erg/s and D is the distance from the object in cm. We have the following given values:

$$L_{star} = 1.01\,\mathrm{L}_\odot \quad L_p = 1.01 \times 10^{-2}\,\mathrm{L}_\odot \quad L_{plow} = 1.01 \times 10^{-3}\,\mathrm{L}_\odot \tag{4.2}$$

$$D_{star} = 19\,\mathrm{au} \quad D_{star2} = 9\,\mathrm{au} \quad D_p = 1\,\mathrm{au} \tag{4.3}$$

where L_{star}, L_p and L_{plow}[1] is the luminosity of the star, luminosity of the planet, and the luminosity of the planet but lowered by a factor 10, respectively. D_{star}, D_{star2} and D_p is the distance from the star to the outer rim for scenario 1, the distance from the star to the outer rim for scenario 2, and the distance from the planet to the outer rim, respectively. Calculating the stellar flux on the outer rim in scenario 1 and 2 and the flux of the planet for L_p and L_{plow} on the outer rim, gives:

$$F_p = 1.37 \times 10^4\,\mathrm{erg/s/cm^2} \tag{4.4}$$

$$F_{plow} = 1.37 \times 10^3\,\mathrm{erg/s/cm^2} \tag{4.5}$$

$$F_{star} = 3.81 \times 10^3\,\mathrm{erg/s/cm^2} \tag{4.6}$$

$$F_{star2} = 1.70 \times 10^4\,\mathrm{erg/s/cm^2} \tag{4.7}$$

Taking the ratio of F_p with respect to F_{star} and F_{star2}, and doing the same for F_{plow} gives:

$$\frac{F_p}{F_{star}} = 3.61 \qquad \frac{F_p}{F_{star2}} = 0.81 \qquad \frac{F_{plow}}{F_{star}} = 0.36 \qquad \frac{F_{plow}}{F_{star2}} = 0.08 \tag{4.8}$$

The smaller the ratio the more dominant the stellar radiation. This shows that decreasing the planet's luminosity by a factor 10 increases the star's influence by a factor of 10. Additionally, placing the planet with CPD at $x = 10\,\mathrm{au}$ increases the star's radiative impact by a factor of $\frac{3.61}{0.81} \approx 4.5$.[2] These are, of course, hefty simplifications, but it serves to further explain our results.

4.2 Concluding remarks on improvements

The inaccuracies, both present for the temperature and the radiation field, were due to the small size of the CPD and the way MCMax3D distributes its photons between multiple light sources. The first case, can only be solved by either increasing the size of the CPD or increasing the number of photons at the cost of longer computation times. The second case, is an indication that MCMax3D needs optimization. The way it works right now, is that for two light sources the total number of photons will be distributed according to their luminosity relative to each other. For our models, we had a star with a stellar luminosity of $L_* = 1.01\,\mathrm{L}_\odot$, and two planetary luminosities ($1.01 \times 10^{-2}\,\mathrm{L}_\odot$ or $1.01 \times 10^{-3}\,\mathrm{L}_\odot$). For the default planetary luminosity ($L_p = 1.01 \times 10^{-2}\,\mathrm{L}_\odot$), we have a ratio of $L_*/L_p = 100$. According to this ratio, MCMax3D will assign a hundred times more photons to the star. So when we used 10^9 photons, the planet (for $L_p = 1.01 \times 10^{-2}\,\mathrm{L}_\odot$) only got to use 1% of all the photons (10^7). As for the radiation field we had a total of 3×10^6 photons, so the planet only used 3×10^4 photons for the default luminosity case, and merely 3×10^3 photons for the low luminosity case. Furthermore, the radiation field comprised the Far-UV spectrum, which has a higher opacity (see Fig. 1.4) than the optical

[1] Normally, the default luminosity and lower luminosity were both indicated with L_p. But in order to properly separate these two cases we used L_{plow} for the low luminosity.

[2] This value could also be obtained by simply taking the ratio of $\frac{F_{star2}}{F_{star}} = \left(\frac{D_{star}}{D_{star2}}\right)^2 = \left(\frac{19}{9}\right)^2 \approx 4.5$. Note that this only works if their luminosities are the same.

spectrum — which is most relevant for the temperature calculation — and is thus more easily absorbed. In terms of computing the radiation field, improvements are clearly necessary: either MCMax3D itself needs to be optimized or we need to upgrade from 32 bit to 64 bit so that a total of $2^{63} \approx 9.2 \times 10^{18}$ photons can be used. The main problem will then be the computation time, however.

Bibliography

Andrews, Sean M. et al. (2018). “The Disk Substructures at High Angular Resolution Project (DSHARP). I. Motivation, Sample, Calibration, and Overview”. In: *The Astrophysical Journal Letters* 869.2, L41, p. L41. DOI: 10.3847/2041-8213/aaf741. arXiv: 1812.04040 [astro-ph.SR].

Armitage, Philip J. (2010). *Astrophysics of Planet Formation.*

Ayliffe, Ben A. and Matthew R. Bate (2009). “Circumplanetary disc properties obtained from radiation hydrodynamical simulations of gas accretion by protoplanets”. In: *Monthly Notices of the Royal Astronomical Society* 397.2, pp. 657–665. DOI: 10.1111/j.1365-2966.2009.15002.x. arXiv: 0904.4884 [astro-ph.EP].

Bagenal, F. et al. (2004). *Jupiter : the planet, satellites and magnetosphere.*

Bryden, G. et al. (1999). “Tidally Induced Gap Formation in Protostellar Disks: Gap Clearing and Suppression of Protoplanetary Growth”. In: *The Astrophysical Journal* 514.1, pp. 344–367. DOI: 10.1086/306917.

Canup, Robin M. and William R. Ward (2002). “Formation of the Galilean Satellites: Conditions of Accretion”. In: *The Astronomical Journal* 124.6, pp. 3404–3423. DOI: 10.1086/344684.

Clarke, Cathie and Bob Carswell (2007). *Principles of Astrophysical Fluid Dynamics.*

Draine, B. T. and F. Bertoldi (1996). “Structure of Stationary Photodissociation Fronts”. In: *The Astrophysical Journal* 468, p. 269. DOI: 10.1086/177689. eprint: astro-ph/9603032.

Draine, Bruce T. (2011). *Physics of the Interstellar and Intergalactic Medium.*

Fraternali, F. (2019). *Notes on astrophysical hydrodynamics.* [Accessed 7-June-2019]. URL: https://nestor.rug.nl/bbcswebdav/pid-9546406-dt-content-rid-17265724_2/courses/STAF3E5.2018-2019.2A/ah.pdf.

Hartmann, Lee et al. (1998). “Accretion and the Evolution of T Tauri Disks”. In: *The Astrophysical Journal* 495.1, pp. 385–400. DOI: 10.1086/305277.

Hayashi, C. (1981). “Structure of the Solar Nebula, Growth and Decay of Magnetic Fields and Effects of Magnetic and Turbulent Viscosities on the Nebula”. In: *Progress of Theoretical Physics Supplement* 70, pp. 35–53. DOI: 10.1143/PTPS.70.35.

Huang, Jane et al. (2018). “The Disk Substructures at High Angular Resolution Project (DSHARP). II. Characteristics of Annular Substructures”. In: *The Astrophysical Journal* 869.2, L42, p. L42. DOI: 10.3847/2041-8213/aaf740. arXiv: 1812.04041 [astro-ph.EP].

Isella, Andrea et al. (2019). “Submillimeter emission associated with candidate protoplanets”. In: *arXiv e-prints*, arXiv:1906.06308, arXiv:1906.06308. arXiv: 1906.06308 [astro-ph.EP].

Kim, K. H. et al. (2013). “TRANSITIONAL DISKS AND THEIR ORIGINS: AN INFRARED SPECTROSCOPIC SURVEY OF ORION A”. In: *The Astrophysical Journal* 769.2, p. 149. DOI: 10.1088/0004-637x/769/2/149. URL: https://doi.org/10.1088%2F0004-637x%2F769%2F2%2F149.

Kley, W. (1999). “Mass flow and accretion through gaps in accretion discs”. In: *Monthly Notices of the Royal Astronomical Society* 303.4, pp. 696–710. DOI: 10.1046/j.1365-8711.1999.02198.x. arXiv: astro-ph/9809253 [astro-ph].

Kley, W. and R. P. Nelson (2012). “Planet-Disk Interaction and Orbital Evolution”. In: *Annual Review of Astronomy and Astrophysics* 50, pp. 211–249. DOI: 10.1146/annurev-astro-081811-125523. arXiv: 1203.1184 [astro-ph.EP].

Kley, Wilhelm (2019). “Planet Formation and Disk-Planet Interactions”. In: *Saas-Fee Advanced Course* 45, p. 151. DOI: 10.1007/978-3-662-58687-7_2.

Korycansky, D. G. et al. (1991). “Numerical models of giant planet formation with rotation”. In: *Icarus* 92.2, pp. 234–251. DOI: 10.1016/0019-1035(91)90048-X.

LeBlanc, Francis (2010). *An Introduction to Stellar Astrophysics.*

Ma, Xiangcheng et al. (2019). “Dust attenuation, dust emission, and dust temperature in galaxies at z $\geq$ 5: a view from the FIRE-2 simulations”. In: *Monthly Notices of the Royal Astronomical Society* 487.2, pp. 1844–1864. DOI: 10.1093/mnras/stz1324. arXiv: 1902.10152 [astro-ph.GA].

Maciel, Walter J. (2013). *Astrophysics of the Interstellar Medium.* DOI: 10.1007/978-1-4614-3767-3.

Min, M., J. Bouwman, et al. (2016). “The abundance and thermal history of water ice in the disk surrounding HD 142527 from the DIGIT Herschel Key Program”. In: *Astronomy & Astrophysics* 593, A11, A11. DOI: 10.1051/0004-6361/201425432. arXiv: 1606.07266 [astro-ph.EP].

Min, M., C. P. Dullemond, et al. (2009). “Radiative transfer in very optically thick circumstellar disks”. In: *Astronomy & Astrophysics* 497.1, pp. 155–166. DOI: 10.1051/0004-6361/200811470. arXiv: 0902.3092 [astro-ph.IM].

Nelson, Richard P. (2018). “Planetary Migration in Protoplanetary Disks”. In: *Handbook of Exoplanets, ISBN 978-3-319-55332-0. Springer International Publishing AG, part of Springer Nature, 2018, id.139*, p. 139. DOI: 10.1007/978-3-319-55333-7_139.

Papaloizou, J. and D. N. C. Lin (1984). “On the tidal interaction between protoplanets and the primordial solar nebula. I - Linear calculation of the role of angular momentum exchange”. In: *The Astrophysical Journal* 285, pp. 818–834. DOI: 10.1086/162561.

Pinte, Christophe (2015). “Continuum radiative transfer”. In: *European Physical Journal Web of Conferences*. Vol. 102, p. 00006. DOI: 10.1051/epjconf/201510200006.

Pollack, J. B. and G. Consolmagno (1984). “Origin and evolution of the Saturn system”. In: *IN: Saturn (A85-33976 15-91). Tucson, AZ, University of Arizona Press, 1984, p. 811-866. Previously announced in STAR as N84-23433.* Ed. by T. Gehrels and M. S. Matthews, pp. 811–866.

Szulágyi, J. et al. (2018). “Observability of forming planets and their circumplanetary discs - I. Parameter study for ALMA”. In: *Monthly Notices of the Royal Astronomical Society* 473, pp. 3573–3583. DOI: 10.1093/mnras/stx2602. arXiv: 1709.04438 [astro-ph.EP].

Ward, William R. and Robin M. Canup (2010). “Circumplanetary Disk Formation”. In: *The Astronomical Journal* 140.5, pp. 1168–1193. DOI: 10.1088/0004-6256/140/5/1168.

Weingartner, J. C. and B. T. Draine (2001). “Dust Grain-Size Distributions and Extinction in the Milky Way, Large Magellanic Cloud, and Small Magellanic Cloud”. In: *The Astrophysical Journal* 548, pp. 296–309. DOI: 10.1086/318651. eprint: astro-ph/0008146.

Woitke, P., I. Kamp, et al. (2009). “Radiation thermo-chemical models of protoplanetary disks. I. Hydrostatic disk structure and inner rim”. In: *Astronomy & Astrophysics* 501.1, pp. 383–406. DOI: 10.1051/0004-6361/200911821. arXiv: 0904.0334 [astro-ph.EP].

Woitke, P., M. Min, et al. (2016a). "Consistent dust and gas models for protoplanetary disks. I. Disk shape, dust settling, opacities, and PAHs". In: *Astronomy & Astrophysics* 586, A103, A103. DOI: 10.1051/0004-6361/201526538. arXiv: 1511.03431 [astro-ph.EP].

— (2016b). "Consistent dust and gas models for protoplanetary disks. I. Disk shape, dust settling, opacities, and PAHs". In: *Astronomy & Astrophysics* 586, A103, A103. DOI: 10.1051/0004-6361/201526538. arXiv: 1511.03431 [astro-ph.EP].

Zhang, Shangjia et al. (2018). "The Disk Substructures at High Angular Resolution Project (DSHARP). VII. The Planet-Disk Interactions Interpretation". In: *The Astrophysical Journal Letters* 869.2, L47, p. L47. DOI: 10.3847/2041-8213/aaf744. arXiv: 1812.04045 [astro-ph.EP].